

# Stress increases sperm respiration and motility in mice and men

Received: 23 October 2023

Accepted: 2 September 2024

Published online: 11 September 2024

 Check for updates

Nickole Moon<sup>1,2</sup>, Christopher P. Morgan<sup>2</sup>, Ruth Marx-Rattner<sup>2</sup>, Alyssa Jeng<sup>1</sup>, Rachel L. Johnson<sup>3</sup>, Ijeoma Chikezie<sup>2</sup>, Carmen Mannella<sup>4</sup>, Mary D. Sammel<sup>3</sup>, C. Neill Epperson<sup>1</sup> & Tracy L. Bale<sup>1,2</sup> ✉

Semen quality and fertility has declined over the last 50 years, corresponding to ever-increasing environmental stressors. However, the cellular mechanisms involved and their impact on sperm functions remain unknown. In a repeated sampling human cohort study, we identify a significant effect of prior perceived stress to increase sperm motility 2-3 months following stress, timing that expands upon our previous studies revealing significant stress-associated changes in sperm RNA important for fertility. We mechanistically examine this post-stress timing in mice using an *in vitro* stress model in the epididymal epithelial cells responsible for sperm maturation and find 7282 differentially H3K27me3 bound DNA regions involving genes critical for mitochondrial and metabolic pathways. Further, prior stress exposure significantly changes the composition and size of epithelial cell-secreted extracellular vesicles that when incubated with mouse sperm, increase mitochondrial respiration and sperm motility, adding to our prior work showing impacts on embryo development. Together, these studies identify a time-dependent, translational signaling pathway that communicates stress experience to sperm, ultimately affecting reproductive functions.

As semen quality and fertility have declined over the last 50 years<sup>1,2</sup>, identifying the processes altering sperm function and physiology is critical. Further, the profound and lasting stress of the COVID-19 pandemic on young adults, i.e., men of reproductive age, has resulted in a significant rise in rates of mental illness<sup>3-6</sup>. Despite reports that stress affects reproductive fitness<sup>7,8</sup>, the underlying cellular and molecular mechanisms responsible for communication of experiential information to germ cells to impact reproductive outcomes and fertility are not understood. The prolonged effects of stress are transmitted long after the trauma or stress ends, indicating that allostasis, or cellular reprogramming that alters basal cellular functions in response to an environmental challenge, has occurred. Though allostasis was first described by Sterling and Eyer<sup>9</sup>, the extensive contributions of Bruce McEwen and others identified that long-term

adaptation following chronic periods of stress induced a new allostatic state, or set point, over time<sup>10-14</sup>.

In males, somatic epididymal epithelial cells (EECs) contribute to processes required for sperm function and fertility<sup>15,16</sup>. EECs secrete a number of factors essential for sperm maturation and motility into the caput lumen, including biological nanoparticles, such as extracellular vesicles (EVs)<sup>17-24</sup>. Previous studies from our lab and others showed that EVs conveyed RNA and protein cargo to sperm, contributing detectable changes in sperm composition many months after stress ended<sup>18-20,25-36</sup>. Further, our lab previously validated an *in vitro* EEC model that recapitulated the primary features of our *in vivo* chronic paternal stress paradigm while allowing for cell-type specific EV collection<sup>25</sup>. We found that changes in EEC secreted EV cargo following, but not during, stress treatment causally affected reproductive

<sup>1</sup>Department of Psychiatry, University of Colorado Anschutz Medical Campus School of Medicine, Aurora, CO 80045, USA. <sup>2</sup>Department of Pharmacology, University of Maryland Baltimore, Baltimore, MD 21201, USA. <sup>3</sup>Department of Biostatistics and Informatics, Colorado School of Public Health, University of Colorado Anschutz Medical Campus, Aurora, CO 80045, USA. <sup>4</sup>Department of Physiology, University of Maryland Baltimore, Baltimore, MD 21201, USA.

✉ e-mail: [tracy.bale@cuanschutz.edu](mailto:tracy.bale@cuanschutz.edu)

and offspring developmental outcomes when sperm had been incubated with these EVs<sup>25</sup>. Therefore, we utilized this system in the current studies to identify the specific molecular mechanisms involved in stress hormone-mediated allostasis, and then tested the functional impact of this timing relationship to determine how stress altered sperm function in mice and men.

While we understand little as to how cells regulate an allostatic state at the molecular level, it is well accepted that changes in energy requirements reflect changes in the basal cellular state<sup>37–39</sup>. As mitochondria are sensitive to stress mediators, including cortisol in humans and corticosterone in mice, and mitochondrial respiration is a primary source of cellular energy, it is postulated that allostasis involves metabolic and mitochondrial mechanisms<sup>37,39–43</sup>. Importantly, among the systemic changes promoted by stress, significant elevations in circulating glucocorticoids discordant with the programmed circadian rhythm are the primary indicators of an organismal stressed state<sup>41,44,45</sup>. The low affinity glucocorticoid receptor (GR) is sensitive to the levels, timing, and duration of glucocorticoids during stress relative to the daily changes that occur with the circadian rhythm found in all mammals<sup>46–48</sup>. Additionally, GR is a key regulator of cellular processes important for mitochondrial and transcriptional functions, placing it in a nodal point for partitioning resources and energy<sup>43,49</sup>. Therefore, we hypothesized that recalibration of an allostatic set point is mediated at the level of mitochondrial and nuclear regulation of cellular energy requirements, resulting in changes to cellular communication. In our EEC model, this would include changes to EVs required for sperm function. As EVs are uniquely positioned to convey signals of changing energy requirements, and as energy is critical to sperm motility, we investigated the role of EVs to directly regulate sperm respiration and motility in mice. Subsequently, we then examined the impact and timing of prior perceived stress on sperm motility in men.

## Results

### Sperm motility increased 2–3 months after perceived stress

As our prior studies identified the timing at which prior perceived stress score (PSS) in men was associated with significant changes in sperm small non-coding RNA (sncRNA) content important for fertility<sup>50</sup>, we hypothesized that prior perceived stress at critical time points may also increase sperm motility in a human cohort. Therefore, we measured the perceived stress score and sperm motility monthly from one to six months by computer automated semen analysis (CASA) in whole ejaculate (Fig. 1a). Demographic data for the 34 healthy participants are reported in Table 1. There was no effect of time or PSS on volume ( $F(5140)=1.24$ ,  $p=0.29$ ; Time -3:  $\beta=-0.003$ ,  $t(108)=-0.47$ ,  $p=0.64$ ), sperm concentration ( $F(5140)=1.07$ ,  $p=0.38$ ; Time -3:  $\beta=-0.0002$ ,  $t(108)=-0.02$ ,  $p=0.98$ ), % motile sperm ( $F(5140)=0.41$ ,  $p=0.84$ , Time -3:  $\beta=0.009$ ,  $t(107)=1.48$ ,  $p=0.14$ ), total sperm count ( $H(5)=9.778$ ,  $p>0.05$ ), or total motile sperm count ( $H(5)=7.784$ ,  $p>0.05$ ; Time -3:  $\beta=0.009$ ,  $t(107)=0.57$ ,  $p=0.57$ ) (Fig. 1b–f; Supplementary Fig. 1a, b, q). Non-parametric analyses were utilized to analyze total sperm count and total motile sperm count due to non-normal residuals (Shapiro-Wilk test,  $W=0.0282$ ,  $p<0.0001$  (total sperm count);  $W=0.905$ ,  $p<0.0001$  (total motile sperm count)). Using mixed effects modeling, we revealed that PSS at Time 0, Time -1, and Time -2 was not associated with average path velocity (VAP) (Time 0:  $\beta=-0.001$ ,  $t(108)=-0.20$ ,  $p=0.84$ ; Time -1:  $\beta=-0.001$ ,  $t(107)=-0.46$ ,  $p=0.65$ ; Time -2:  $\beta=0.003$ ,  $t(107)=1.02$ ,  $p=0.31$ ), curvilinear velocity (VCL) (Time 0:  $\beta=-0.002$ ,  $t(108)=-0.62$ ,  $p=0.54$ ; Time -1:  $\beta=0.001$ ,  $t(107)=0.31$ ,  $p=0.76$ , Time -2:  $\beta=0.002$ ,  $t(107)=0.72$ ,  $p=0.47$ ) or straight line velocity (VSL) (Time 0:  $\beta=0.001$ ,  $t(108)=0.25$ ,  $p=0.81$ ; Time -1:  $\beta=-0.0003$ ,  $t(107)=-0.10$ ,  $p=0.92$ ; Time -2:  $\beta=0.005$ ,  $t(107)=1.67$ ,  $p=0.09$ ) at the time of the collection (Fig. 1g–i; Supplementary Fig. 1d–p). However, PSS at Time -3 was significantly associated with all three sperm velocities, VAP ( $\beta=0.006$ ,

$t(107)=2.43$ ,  $p<0.05$ ), VCL ( $\beta=0.006$ ,  $t(107)=2.09$ ,  $p<0.05$ ) and VSL ( $\beta=0.008$ ,  $t(107)=3.09$ ,  $p<0.01$ ) (Fig. 1j, Supplementary Fig. 1n–p). Additionally, percent progressive motile sperm was significantly and positively associated with PSS at Time -3 (% Progressive Motile:  $\beta=0.008$ ,  $t(107)=2.24$ ,  $p<0.05$ ) (Supplementary Fig. 1r). For all models we controlled for age, days since ejaculation prior to sample collection and the site of sample collection, either at home or at the study site.

### Prior treatment dramatically reprograms H3K27me3 binding

As our work here found that prior stress is associated with critical sperm functions, we examined the hypothesis that prior stress regulates cells required for sperm maturation. We previously identified the ubiquitous transcriptional repressor H3K27me3 as a stress-responsive histone modification in the caput epididymis<sup>25</sup>, therefore, we examined the hypothesis that a new allostatic set point is maintained by lasting changes in H3K27me3 distribution. To assess these effects in a specific cell population, we utilized our validated model assessing the post-corticosterone treatment effects in epididymal epithelial cells (EECs) (Fig. 2a). Briefly, confluent mouse distal caput EECs were treated with corticosterone for 72 hours, subsequent media changes washed out the treatment, and at the post-corticosterone time point six days later, we implemented the high efficiency epigenetic profiling approach, Cleavage Under Targets and Release Using Nuclease sequencing (CUT&RUN) (Fig. 2a, b). We found more than 50% of H3K27me3-binding loci were associated with gene promoter regions (Fig. 2c, Supplementary Fig. 2a) and within 5Kb of the transcription start sites (Fig. 2d). Differential binding analysis using the Diffbind package revealed 7282 differentially bound regions by H3K27me3 between post-corticosterone and post-vehicle EECs at the day 9 timepoint (Fig. 2a), representing 7135 enriched regions and only 147 H3K27me3 depleted regions (Fig. 2e, f, Supplementary Fig. 2b). Principal component analysis revealed that 70% of the variance between samples was attributed to principal component (PC) 1, which delineated the treatment groups (Supplementary Fig. 2c). Thirteen percent of variance was attributed to PC2, and was largely driven by two post-corticosterone samples (Supplementary Fig. 2c). Furthermore, H3K27me3 bound loci were associated with genes involved in mitochondrial organization among other metabolic and catabolic processes as determined by Gene Set Enrichment Analysis (Fig. 2g).

### Transcriptional networks regulate the allostatic trajectory

To determine whether reprogramming at the level of the chromatin regulated gene expression patterns following treatment, we analyzed co- and differentially regulated RNA expression at subsequent media changes in our model (Fig. 3a). Across all time points, 13129 genes were identified after filtering for features present in all samples (CPM > 1 in 4 samples) (Fig. 3b) and analyzed with weighted gene co-expression network analysis (WGCNA). The dynamic tree cutting algorithm revealed 11 modules of genes co-regulated by either treatment or time ranging in size from 179 to 4418 genes (Supplementary Fig. 3a). We used the topological overlap matrix to visualize the hierarchical clustering of all genes across time and treatment (Supplementary Fig. 3b). The 11 modules representing clusters of highly correlated genes, the module correlation with time and treatment, and the respective  $p$  values are summarized in Fig. 3c. Expression of co-regulated genes in the pink module exhibited the strongest correlation to prior corticosterone treatment with a correlation coefficient of 0.74 ( $p<0.0001$ ) (Fig. 3c). Therefore, we utilized functional annotation analysis of the genes comprising the pink module to determine the top biological processes associated with those genes and revealed significant associations with gene ontology (GO) terms including mitochondrial ATP synthesis coupled proton transport (FDR = < 0.0001, Fold Enrichment = 24.94) and mitochondrial respiratory chain complex I assembly (FDR = < 0.0001, Fold Enrichment = 19.03) (Fig. 3d; Supplementary

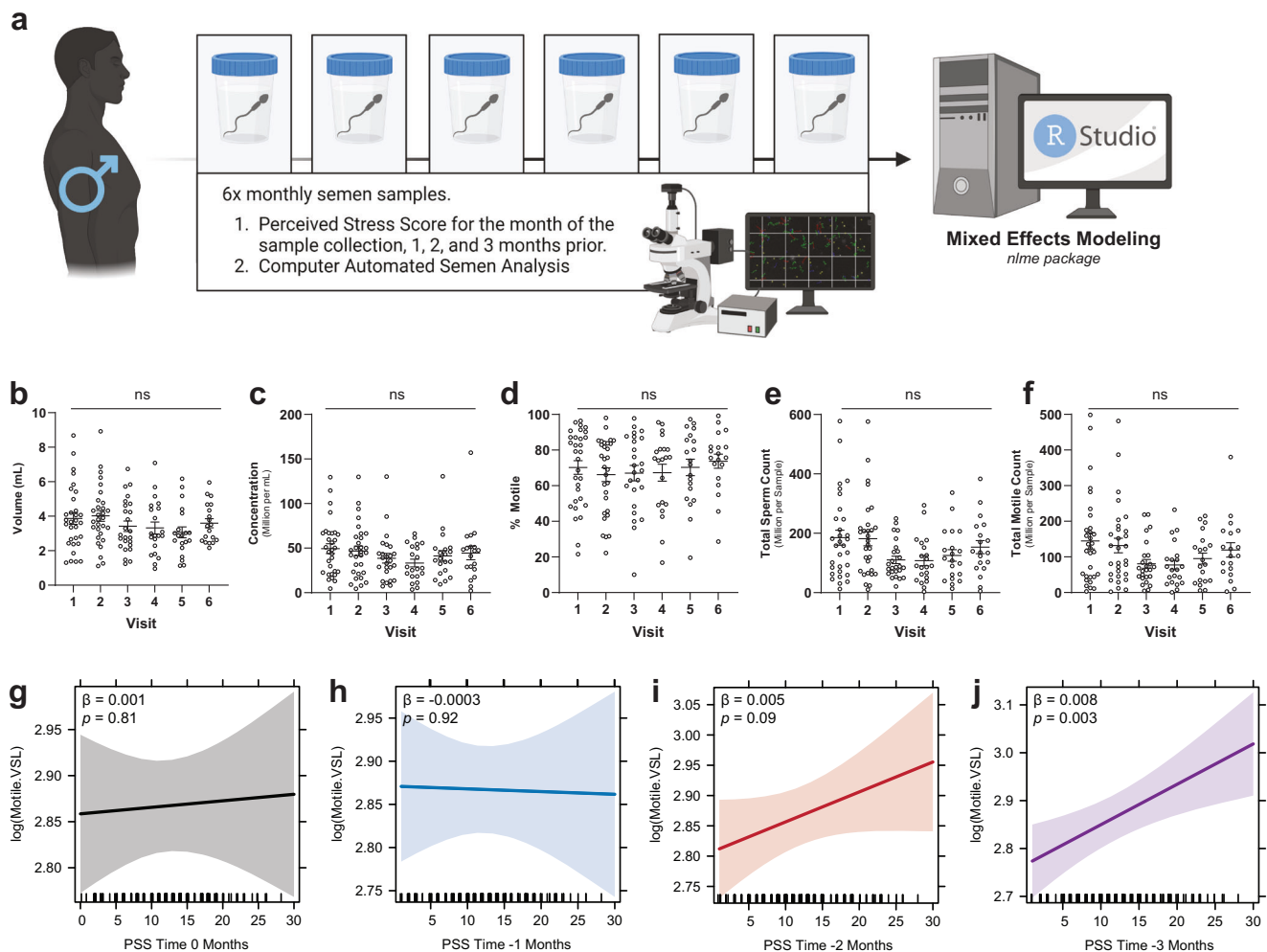


**Fig. 1 | Sperm motility increased 2-3 months following elevated perceived stress in healthy men.** **a** Schematic of the human cohort study. Briefly, whole ejaculate was collected for one to six months, and Perceived Stress Score (PSS) was reported for the month of each collection (Time 0), as well as one month (Time -1), two months (Time -2), and three months (Time -3) prior to each collection. At each collection, sperm motility was measured by computer automated semen analysis (CASA) in fresh whole ejaculate. The association between prior PSS and motility was modeled using mixed effects modeling by the *nlme* package. **b-f** Whole ejaculate volume, concentration, % motile sperm, total sperm count, and total motile sperm count (TMC) across all visits.  $N = 34$  participants, each providing one monthly semen sample for up to six months. Data are mean  $\pm$  SEM; one-way analysis of variance demonstrates no significant changes in volume, concentration or % motile sperm. Kruskal-Wallis test demonstrates no significant changes in (e) total sperm count or (f) total motile sperm count. **g** Models of the association between PSS at

Time 0 and VSL ( $\beta = 0.001$ ,  $t(108) = 0.25$ ,  $p = 0.81$ ) at collection. **h** Models of the association between PSS at Time -1 and VSL ( $\beta = -0.0003$ ,  $t(107) = -0.10$ ,  $p = 0.92$ ) at collection. **i** Models of the association between PSS at Time -2 and VSL ( $\beta = 0.005$ ,  $t(107) = 1.67$ ,  $p = 0.09$ ) at collection. **j** Models of the association between PSS at Time -3 and VSL ( $\beta = 0.008$ ,  $t(107) = 3.09$ ,  $p < 0.01$ ) at collection. For **g**,  $N = 34$  across 146 observations, and for **h-j**,  $N = 34$  across 145 observations due to one missed visit by a participant. For all models, slope significance was tested by a two-sided *t*-test per the standard *nlme* package, shaded gray (**g**), blue (**h**), red (**i**), and purple (**j**) regions reflect the SEM and tick marks on the x-axis denote individual PSS for each observation. Source data are provided as a Source Data file. Figure 1a created with BioRender.com released under a Creative Commons Attribution-NonCommercial-NoDerivs 4.0 International license (<https://creativecommons.org/licenses/by-nc-nd/4.0/deed.en>).

Data 1). Supplementary Data 1 provides all GO terms and related genes associated with the pink module. The turquoise module was also significantly associated with prior corticosterone treatment, but not time (Fig. 3c). Functional annotation analysis of the turquoise module demonstrated genes were significantly associated with biological processes including the cell cycle (FDR = < 0.0001, Fold Enrichment = 2.25) and cell division (FDR = < 0.0001, Fold Enrichment = 2.45) (Supplementary Data 2). Finally, the blue module was only significantly associated with time (Fig. 3c) and contained genes associated with biological processes such as cytoplasmic translation (FDR = < 0.0001, Fold Enrichment = 7.17) (Supplementary Data 3).

Next, we visualized relationships in gene expression patterns between samples by principal component analysis (PCA), revealing that component 1 accounted for 42.7% and component 2 accounted for 22.8% of the variance, corresponding with treatment and time

respectively (Fig. 3e). Unbiased hierarchical clustering by gene expression clustered groups by treatment, except at day 9 when post-corticosterone treatment samples clustered with day 3 control samples (Fig. 3b, e). To understand the gene expression patterns of day 9 post-corticosterone treatment and vehicle treatment, we used differential expression analysis and uncovered 272 differentially expressed genes (DEGs) across two clusters of co-regulated genes, with down-regulation of 187 DEGs (Fig. 3f).

### Decreased cellular energy requirements maintain allostasis

As the chromatin binding and transcriptional network analyses identified mitochondrial processes as allostatic regulators, we confirmed that prior corticosterone exposure functionally affected mitochondrial energy requirements in our *in vitro* model (Fig. 4a). Using whole cell respirometry to measure the oxygen consumption rate

**Table 1 | Demographic information for human cohort**

Number of participants	34
Total number of observations	146
Age, mean (SD)	27.85 (4.72)
Race: <i>n</i> (%)	
White	25 (73.53)
Asian	5 (14.71)
Native American/American Indian	1 (2.94)
More than one race: White & Asian	3 (8.82)
Hispanic or Latino: <i>n</i> (%)	
Yes	4 (11.76)
No	30 (88.24)
Education: <i>n</i> (%)	
Some College	4 (11.76)
Associate Degree	2 (5.88)
College Graduate	7 (20.59)
Some Graduate/Professional School	8 (23.53)
Graduate/Professional Degree	13 (38.24)
Total Household Income, mean (SD)	85093.75 (61199.5)
Current Employment: <i>n</i> (%)	
Full Time	20 (58.82)
Part Time	2 (5.88)
Unemployed	2 (5.88)
Student	9 (26.47)
Armed Forces	1 (2.94)
Collection Location: no. of visits (%)	
Home	103 (70.55)
Study Site	43 (29.45)
Abstinence in days, mean (SD)	3.37 (2.34)
Semen Sample Characteristics, mean (SD)	
Volume (mL)	3.60 (1.60)
Concentration (10 <sup>6</sup> sperm/mL)	42.96 (28.36)
Total Motile Count (10 <sup>6</sup> sperm)	111.30 (96.00)

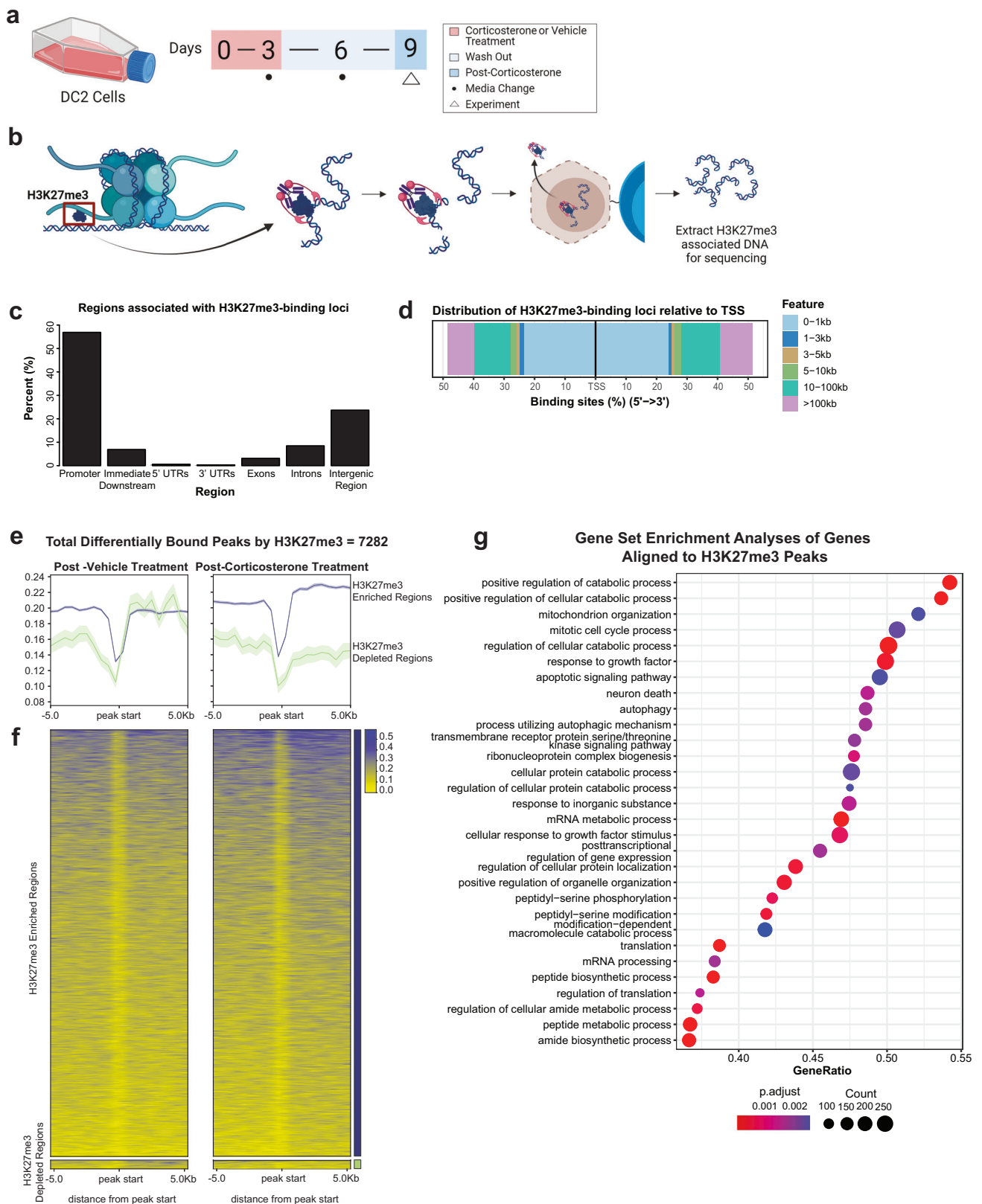
throughout the Mito Stress Test in post-corticosterone EECs (Fig. 4b), we revealed prior treatment decreased basal mitochondrial respiration ( $t(21) = 7.539$ ,  $p < 0.0001$ ) (Fig. 4c), total ATP production rate ( $t(21) = 8.406$ ,  $p < 0.0001$ ) (Fig. 4d), oxidative ATP production rate ( $t(21) = 8.471$ ,  $p < 0.0001$ ) (Fig. 4e), and spare respiratory capacity ( $t(21) = 4.236$ ,  $p = 0.0004$ ) (Supplementary Fig. 4a). While extracellular acidification rate was decreased ( $t(21) = 4.514$ ,  $p = 0.0002$ ) (Supplementary Fig. 4b), there was no change in glycolytic ATP production rate ( $t(21) = 1.687$ ,  $p = 0.8649$ ) (Supplementary Fig. 4c) calculated from respirometry data as previously described<sup>51</sup>. This oxidative respiratory phenotype was conserved when limiting glycolytic substrates glutamine and pyruvate in the respirometry media ( $F_{Stress}(1,43) = 74.08$ ,  $p < 0.0001$ ;  $F_{Substrate}(1,43) = 57.91$ ,  $p < 0.0001$ ;  $F_{Stress*Substrate}(2,43) = 1.765$ ,  $p = 0.1834$ ) (Supplementary Fig. 4d, e). Transmission electron microscopy (TEM) confirmed that mitochondrial ultrastructure reflected changes observed by whole cell respirometry. TEM micrographs, represented by images in Supplementary Fig. 4f-i, revealed the proportion of EEC mitochondria with orthodox relative to condensed ultrastructure was increased following treatment ( $X^2(1500) = 6.406$ ,  $p = 0.01$ ) (Supplementary Fig. 4j), the former associated with slower respiration in isolated mitochondria<sup>52</sup>. This was quantified as decreased mean mitochondrial gray value ( $t(557) = 6.566$ ,  $p < 0.0001$ ) (Supplementary Fig. 4k), and ultrastructure score ( $t(498) = 2.542$ ,  $p = 0.01$ ) (Supplementary Fig. 4l) calculated by assigning orthodox mitochondria (narrower cristae, expanded matrix) a

score of 1 and condensed mitochondria (dilated cristae, darker matrix) a score of 2. There were no differences in mitochondrial area, perimeter, or circularity (Supplementary Fig. 4m-o).

Regulation of mitochondrial allostatic changes by the glucocorticoid receptor (GR) following treatment in EECs was first assessed by evaluating the compartmentalization of GR. We found GR protein was decreased in the nuclear fraction ( $t(4) = 3.3994$ ,  $p = 0.0162$ ) (Supplementary Fig. 5h) and increased in the mitochondrial fraction at day 9 ( $t(6) = 2.218$ ,  $p = 0.0342$ ) (Supplementary Fig. 5i). To examine the role of GR in regulating basal mitochondrial respiration, we expressed short hairpin RNA (shRNA) to reduce GR expression ( $F(2,15) = 8.092$ ,  $p = 0.0041$ ; with the Tukey post-hoc test between empty vector and reduced GR expression,  $p = 0.0037$ , and non-targeted shRNA and reduced GR expression,  $p = 0.0379$ ) (Supplementary Fig. 5a, b) throughout the entire experimental timeline and the measured oxygen consumption rate during the Mito Stress Test. While the previously observed hypo-respiratory phenotype was conserved in empty vector and non-targeted shRNA groups ( $F_{Stress}(1,60) = 61.23$ ,  $p < 0.0001$ ;  $F_{GR\ expression}(2,60) = 275.1$ ,  $p < 0.0001$ ;  $F_{Stress*GR\ expression}(2,60) = 23.38$ ,  $p < 0.0001$  with Tukey post-hoc test between empty vector post-vehicle and post-corticosterone EECs,  $p < 0.0001$ , and non-targeted shRNA post-vehicle and post-corticosterone EECs,  $p = 0.0005$ ), reducing GR expression eliminated the difference in basal mitochondrial respiration observed in EECs following treatment (Tukey post-hoc test between post-vehicle and post-corticosterone EECs with reduced GR expression,  $p = 0.9997$ ) (Supplementary Fig. 5c). Importantly, respiration was reduced in the post-vehicle EECs with reduced GR expression compared to the post-vehicle empty vector and non-targeted shRNA groups (Tukey post-hoc test between post-vehicle EECs with reduced GR expression and empty vector post-vehicle EECs,  $p < 0.0001$ , and post-vehicle EECs with reduced GR expression and non-targeted shRNA post-vehicle EECs,  $p < 0.0001$ ) (Supplementary Fig. 5c).

To temporally resolve the role of GR as a regulator of lasting mitochondrial allostatic changes, we exposed EECs to the GR antagonist RU-486 for 72 hours from days 6 to 9 (Supplementary Fig. 5d). There was no difference in the mitochondrial respiration of RU-486 exposed EECs post-corticosterone treatment compared to the vehicle equivalent ( $F_{Stress}(1,64) = 35.92$ ,  $p < 0.0001$ ;  $F_{RU-486\ exposure}(1,64) = 21.20$ ,  $p < 0.0001$ ;  $F_{Stress*RU-486\ exposure}(1,64) = 23.38$ ,  $p = 0.0003$ ; with the Tukey post-hoc test between post-vehicle/RU-486 treated EECs and post-corticosterone/RU-486 treated EECs at  $p = 0.4024$ ) (Supplementary Fig. 5e). As expected, the hypo-respiratory phenotype was conserved in the control comparison (Tukey post-hoc test between post-vehicle/control treated EECs and post-corticosterone/control treated EECs,  $p < 0.0001$ ) (Supplementary Fig. 5e). In contrast, when EECs were exposed to the GR antagonist RU-486 for 72 hours from days 3 to 6 immediately following treatment, the day 9 mitochondrial respiration was reduced ( $F_{Stress}(1,66) = 102.7$ ,  $p < 0.0001$ ;  $F_{RU-486\ exposure}(1,66) = 11.09$ ,  $p = 0.0014$ ;  $F_{Stress*RU-486\ exposure}(1,66) = 9.160$ ,  $p = 0.0035$ ; with Tukey post-hoc test between post-vehicle/day 3 RU-486 treated EECs and post-corticosterone/day 3 RU-486 EECs,  $p < 0.0001$ ) (Supplementary Fig. 5f, g).

To determine the oxidative mitochondrial mechanism regulating hypo-respiration following corticosterone treatment, we assessed the change in respiration (dOCR) after permeabilizing membranes with recombinant perfringolysin O and injecting the substrates supplying NADH or FADH to the two-electron transport chain entry enzymes, mitochondrial complex I and II (Fig. 4f, g). dOCR was decreased in EECs with prior treatment following injections of glutamate and malate ( $t(15) = 5.770$ ,  $p < 0.0001$ ), and pyruvate and malate ( $t(16) = 3.896$ ,  $p = 0.0013$ ), that supply complex I with NADH, but not alpha-ketoglutarate and malate (Fig. 4h-j). dOCR was not decreased following succinate injection, which supplies complex II with FADH (Fig. 4k). Furthermore, treatment reduced EEC complex I enzyme activity, as determined by oxidation



of NADH to NAD<sup>+</sup> by complex I ( $t(8) = 3.446$ ,  $p = 0.0087$ ) (Fig. 4l). Additionally, Ndufa1 protein, a subunit required for complex I association with the mitochondrial inner membrane and proton translocation<sup>53-56</sup>, was reduced following treatment ( $t(5) = 2.837$ ,  $p = 0.0364$ ) (Fig. 4m).

**EV cargo increased sperm energy requirements and motility**  
 As EVs serve as key intercellular signaling particles that convey corticosterone-sensitive cargo<sup>25</sup>, we examined the hypothesis that corticosterone-mediated changes in the EEC allostatic set point alter bioactive EV cargo to convey signals regarding energy homeostasis

**Fig. 2 | Prior stress dramatically increases H3K27me3 binding distribution using CUT&RUN sequencing analysis.** **a** Schematic of our previously established EEC in vitro post-corticosterone paradigm with treatment beginning at confluency (day 0). Colors indicate: The treatment period (red), the wash out period (light-blue), and the post-corticosterone timepoint (dark-blue) when CUT&RUN was performed. Black circles indicate media changes. **b** The CUT&RUN mechanism where protein A/G-MNase cleaves DNA bound by the ubiquitous transcriptional repressor, H3K27me3, and DNA is extracted for sequencing. **c** Percent of differentially bound H3K27me3 loci detected in all samples within specific components of the nearest gene and **(d)** the distribution of loci relative to the transcription start site (TSS). Color represents the distance from the TSS. Panels **c** and **d** summarize all 7282 peaks identified as differentially bound and do not depend on the magnitude of binding in any individual sample. **e** Representative summary plots of H3K27me3 binding in representative samples on day 9. Blue lines represent the H3K27me3-

enriched cluster peaks. The green line represents the H3K27me3-depleted peaks. Shading represents the SEM. **f** Heatmap of 7282 differentially bound loci post-treatment in one representative sample from each group. Rows reflect individual peaks, and columns reflects a base pair up to 5 Kb from the beginning of the peak. Dark blue indicates enrichment relative to yellow. For the differential binding analysis represented in **e**, **f**,  $N = 4$  in post-vehicle and 5 in post-corticosterone treatment group;  $FDR < 0.05$ . **g** Gene set enrichment analysis of the genes aligning with H3K27me3-associated features. For the top 30 pathways, the node size corresponds to count while node color corresponds with statistical significance (adjusted  $p$ -value, utilizing the “BH” method).  $N = 4$  in post-vehicle and 5 in post-corticosterone treatment groups. Figure 2a,b created with BioRender.com released under a Creative Commons Attribution-NonCommercial-NoDerivs 4.0 International license (<https://creativecommons.org/licenses/by-nc-nd/4.0/deed.en>).

and to regulate mitochondria in target cells. EVs were isolated from media of EEC cultures at the post-corticosterone (cort-EEC EVs) or vehicle (vehicle-EEC EVs) treatment timepoint (Fig. 5a). Nanoparticle tracking analysis revealed that cort-EEC EVs were characterized by smaller median EV size ( $t(14) = 2.945$ ,  $p = 0.0106$ ) (Fig. 5b, d) as we have previously reported<sup>25</sup>. There was no difference in the area under the curve analysis of the EV concentration distribution (Fig. 5b, c). Whole cell respirometry demonstrated that exposure of control EECs to cort-EEC EVs (Supplementary Fig. 6a), decreased day 9 basal mitochondrial respiration ( $t(42) = 15.75$ ,  $p < 0.0001$ ), ATP production rate ( $t(42) = 13.23$ ,  $p < 0.0001$ ), oxidative ATP production rate ( $t(42) = 14.95$ ,  $p < 0.0001$ ), and extracellular acidification rate ( $t(42) = 3.951$ ,  $p < 0.001$ ) (Supplementary Fig. 6b–e).

Given the influence of corticosterone-mediated changes in EV cargo on EEC respiration and the known role for EEC EVs in sperm maturation, we assessed the effect of EV cargo on sperm mitochondrial respiration by incubating cauda sperm with cort- or vehicle-EEC EVs prior to whole cell respirometry (Fig. 5e). Incubating sperm with cort-EEC EVs increased basal mitochondrial respiration ( $t(12) = 2.401$ ,  $p = 0.0334$ ) (Fig. 5f), extracellular acidification rate ( $t(12) = 8.311$ ,  $p < 0.0001$ ) (Fig. 5g), ATP production rate ( $t(12) = 3.170$ ,  $p = 0.0081$ ) (Fig. 5h), and glycolytic ATP production rate ( $t(12) = 8.617$ ,  $p < 0.0001$ ) (Fig. 5i).

As our findings here revealed that prior perceived stress increased sperm motility in men, we assessed the functional impact of cort-EEC EV mediated increases in mitochondrial respiration utilizing Computer Assisted Sperm Analysis (CASA) to evaluate mouse sperm motility parameters following cort-EEC EV incubation (Fig. 5j). CASA revealed cort-EEC EV exposure increased sperm curve velocity (VCL) ( $t(13) = 3.532$ ,  $p = 0.0037$ ), average path velocity (VAP) ( $t(13) = 3.023$ ,  $p = 0.0098$ ), and linear velocity (VSL) ( $t(13) = 2.752$ ,  $p = 0.0165$ ) (Fig. 5k–m). There were no differences in the percent of motile sperm ( $t(13) = 1.444$ ,  $p = 0.1724$ ), either progressive ( $t(13) = 0.3698$ ,  $p = 0.7175$ ) or non-progressive ( $t(13) = 1.475$ ,  $p = 0.1639$ ), or percent of immotile sperm ( $t(13) = 1.444$ ,  $p = 0.1724$ ) (Supplementary Fig. 7a–d). Analysis of the motile sperm population revealed significantly increased VCL ( $t(12) = 2.647$ ,  $p = 0.0213$ ), non-significantly increased VAP ( $t(13) = 1.999$ ,  $p = 0.0670$ ), and VSL ( $t(13) = 1.831$ ,  $p = 0.0901$ ) similar to the significantly increased VCL, VSL, and VAP observed in the total sperm population (Supplementary Fig. 7e–g) (Fig. 5k–m).

## Discussion

The lasting effects of chronic stress on health and disease over the lifespan and across generations are well documented in humans and model organisms<sup>57–77</sup>. However, the impact of stress on germ cells, fertility, and the mechanisms underlying the transmission of parental stress experiences across generations are not well understood. As defined by Bruce McEwen, the lasting cellular changes affected by stress are driven by allostasis, the ability to adapt to stress and achieve stability through change<sup>10–13,39,40,78</sup>. When homeostatic mediators, such

as glucocorticoids, are dysregulated by trauma or in a chronic stress state, they promote a lasting change in basal cellular functions<sup>13,37,79</sup>. While previous studies have identified secreted cellular nanoparticles, extracellular vesicles, as a source for signaling metabolic changes altered by stress to other cells and tissues, how an allostatic state alters downstream sperm function over time is unclear.

To determine the impact and timing of prior perceived stress on sperm function, we assessed sperm motility in a repeated collection healthy human cohort study. Amazingly, there was a direct and significant positive association between sperm velocity (curvilinear velocity (VCL), average path velocity (VAP), and straight-line velocity (VSL)), percent progressive motile sperm, and perceived stress at time -3 months, but no associations the same or one month prior to the collection, replicating findings in the mouse study reported here. Further, these human cohort data are also consistent with our previous findings showing a similar timeframe, as early as three months following increased perceived stress, for significant changes in specific sperm small non-coding RNA across subjects, including microRNA, piRNA, and tRNA fragments<sup>50</sup>. Critically, increases in percent progressive motile sperm, and sperm velocity have been associated with increased fertility<sup>2,80,81</sup>. While the current sample is a subset of participants from an ongoing study and the study design is limited in its ability to assess fertility and reproductive consequences associated with fertility, the finding that prior perceived stress influenced sperm motility is key in the context of a current global decline in fertility that is partially attributed to a decline in semen quality and increases in male factor infertility<sup>2,82,83</sup>. By understanding the mechanisms that promote these changes in motility, novel therapeutics that assist couples struggling to conceive can be developed. Together, these findings suggest that cellular allostatic changes are communicated to sperm and provide signals and cargo able to impact sperm function and may ultimately alter reproductive fitness.

To determine the somatic cellular mechanism responsible for interpreting and communicating prior stress experience to sperm, we assessed the ubiquitous transcriptional repressive mark, H3K27me3, that we previously established as a stress-responsive histone modification in the mouse epididymis<sup>25</sup>, distinguishing H3K27me3 as a key target to begin to probe the lasting contributions of epigenetics on allostasis post-corticosterone treatment. Therefore, we utilized CUT&RUN sequencing as an advanced molecular strategy to assess the distribution of H3K27me3 across the EEC chromatin, hypothesizing that following corticosterone treatment we should detect an increase in this mark. In fact, differential binding analysis revealed a substantial increase in H3K27me3 binding at over 7000 loci following treatment, likely contributing to the significant reduction in EEC gene expression detected by post-corticosterone treatment day 9. Additionally, our gene set enrichment analyses (GSEA) revealed H3K27me3-associated genes were highly involved in mitochondrial and metabolic processes, again confirming the linkage between epigenetic and mitochondrial allostatic programming. Given the decrease in nuclear GR in EECs post-

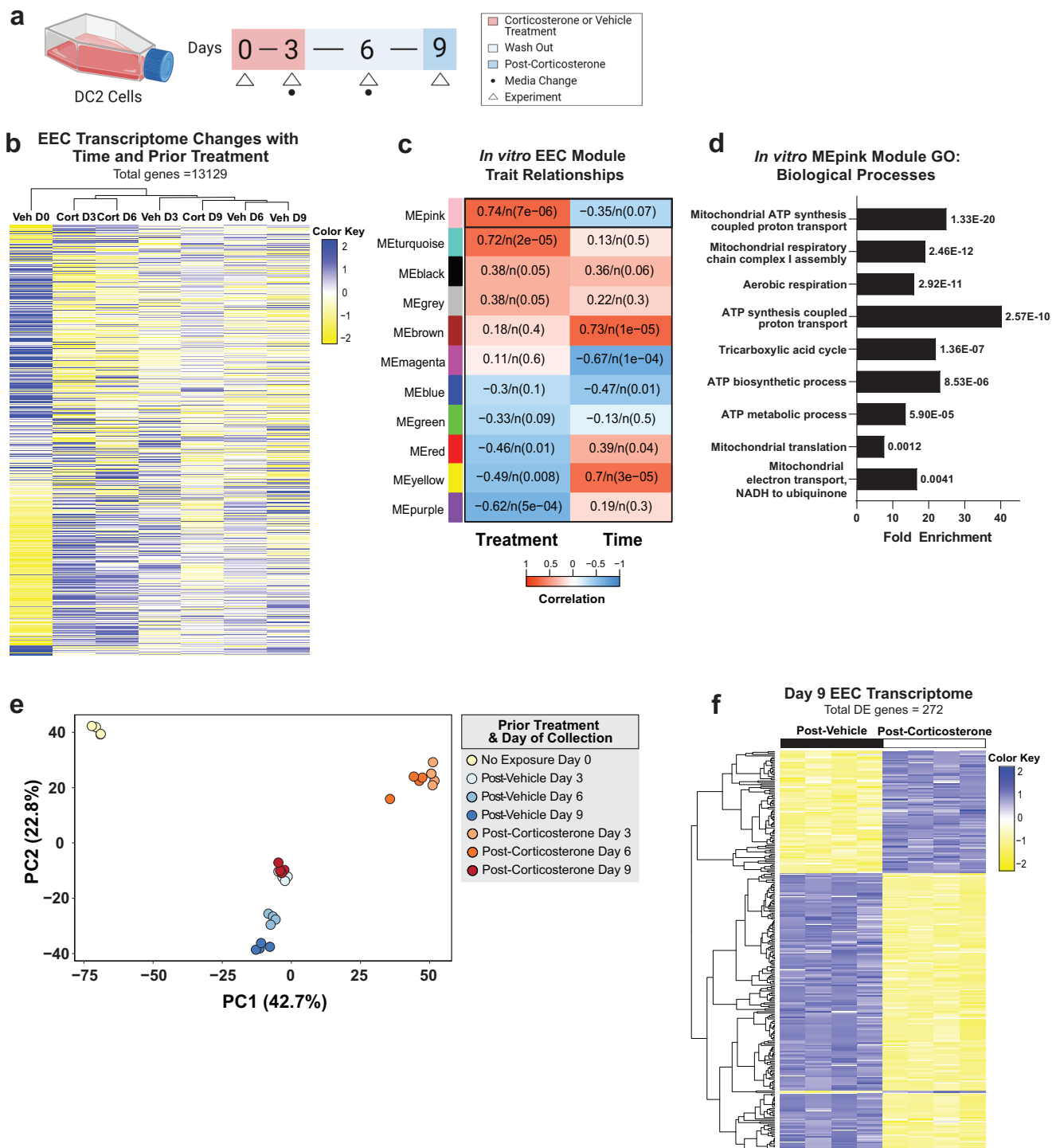
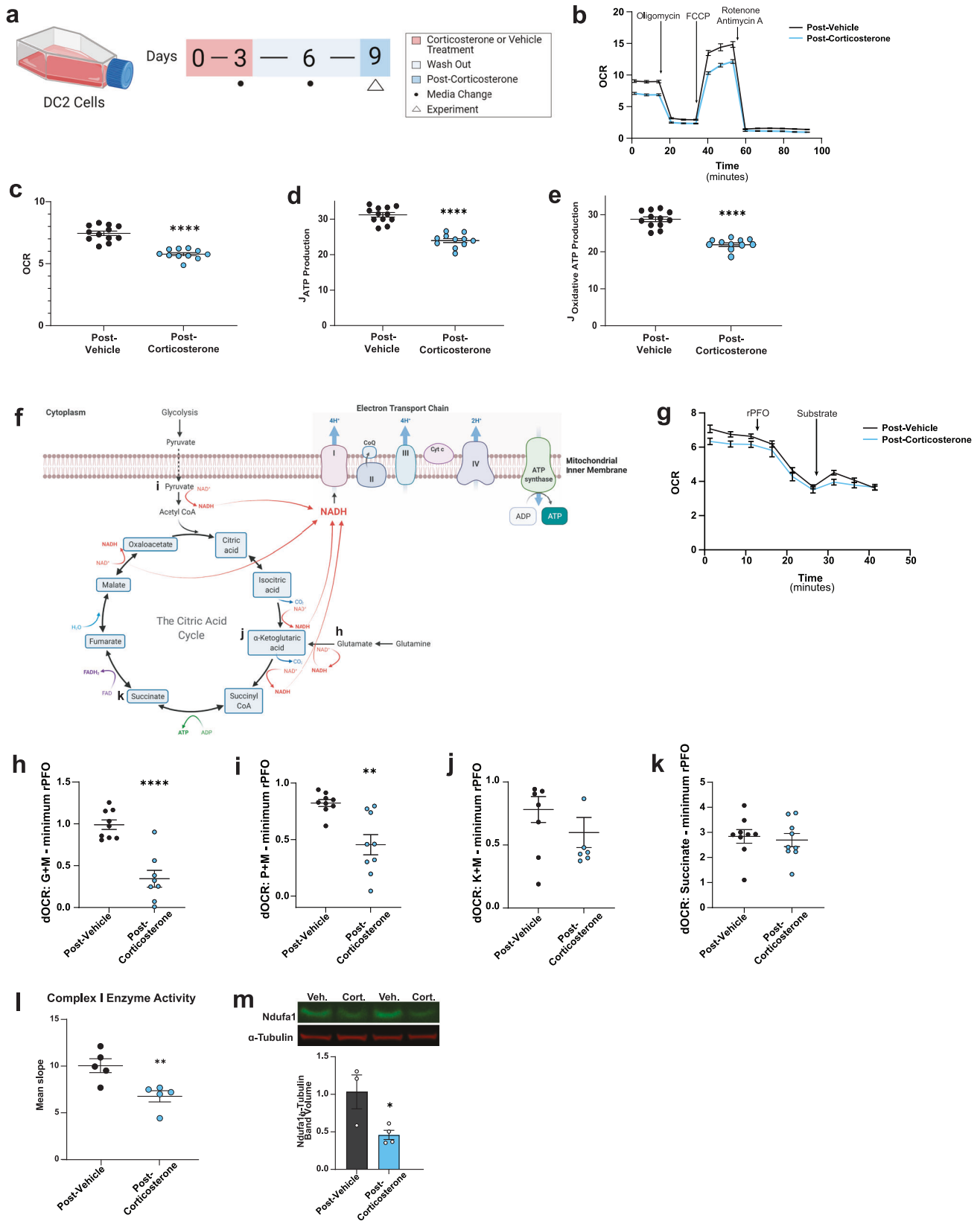


**Fig. 3 | Co-regulation of transcriptional networks preceded transcriptional downregulation, indicating that prior corticosterone treatment influenced the trajectory of a cellular allostastic set point. a** Confluent EEC cultures were exposed to our *in vitro* post-corticosterone paradigm. RNA was isolated before treatment at day 0 (confluency), at the end of treatment (day 3), and at subsequent media exchanges during the wash-out period (days 6 and 9), denoted by white arrows. Circles indicate media exchanges. **b** Heatmap of all genes from RNA-sequencing of EEC RNA isolated at the denoted timepoints. Unbiased hierarchical clustering of samples is visualized by dendrogram. **c** Module-trait associations between module eigengenes calculated from gene expression patterns in the EEC dataset and time or treatment. Rows correspond to a module eigengene while columns align with time or treatment. Color designates the correlation according to the legend. Pearson correlation and *p* value for each module are presented. **d** The

top ten significant biological processes identified by functional analysis of genes in the MEpink module. FDR is presented in line with each bar. **e** RNA-seq expression data were assessed by principal component analysis which revealed that component 1 accounts for 42.7% of the variance and aligns with treatment while component 2 accounts for 22.8% of variance and aligns with maturation ( $N = 4$  plates). Color represents treatment group. **f** Differential expression analyses revealed 272 DEGs between day 9 post-corticosterone and post-vehicle samples visualized by heatmap. Hierarchical clustering of samples visualized by dendrogram ( $N = 4$  plates, adjusted  $p < 0.05$ ,  $p$  value adjustment method = “BH”). Source data are provided as a Source Data file. Figure 3a created with BioRender.com released under a Creative Commons Attribution-NonCommercial-NoDerivs 4.0 International license (<https://creativecommons.org/licenses/by-nc-nd/4.0/deed.en>).



corticosterone treatment and the known role of GR to regulate chromatin organization through the recruitment of histone modifying enzymes and direct association with other epigenetic and DNA bound factors, upregulation of H3K27me3 may result from a decrease in direct or indirect interactions of GR with H3K27me3, or with other regulatory factors in the nucleus<sup>49,84-86</sup>. Furthermore, in accord with

the known stoichiometric constraints on post-translational histone modifications<sup>87</sup>, we posit that dramatic changes in the ubiquitous repressive mark, H3K27me3, likely reflect the coordinated redistribution of many histone modifications across the genome to influence gene expression, in part controlling mitochondrial genes, in a new allostatic setpoint. While our study examined H3K27me3, previous

**Fig. 4 | Cellular allostatic set point maintained decreased basal energy requirements and ATP production rates driven by decreased mitochondrial complex I function.** **a** Schematic of the timeline for our EEC in vitro corticosterone treatment paradigm. **b** Representative Mito Stress Test data where cultures were exposed to oligomycin, FCCP, and rotenone and antimycin A.  $N = 12$  in post-vehicle and 11 in post-corticosterone treatment group. **c** Baseline mitochondrial oxygen consumption rate (OCR).  $N = 12$  in the post-vehicle and 11 in the post-corticosterone treatment group, two-sided  $t$ -test, \*\*\*\* $p < 0.0001$ . **d, e** Total and oxidative ATP production rates.  $N = 12$  in post-vehicle and 11 in post-corticosterone treatment group; two-sided  $t$ -test, \*\*\*\* $p < 0.0001$ . **f** Schematic of the citric acid cycle and electron transport chain contributions to oxidative respiration. Red arrows emphasize how substrates contribute NADH for complex I activity. Letters annotate the corresponding panel. **g** Representative Seahorse experiment in which EEC cultures were permeabilized with recombinant perfringolysin O, followed by one of the following: glutamate and malate, pyruvate and malate, alpha-ketoglutarate and malate, or succinate.  $N = 9$  in the post vehicle and 8 in the post-corticosterone treatment group. The change in OCR ( $\Delta$ OCR) was significantly less in post-

corticosterone EECs following injection of glutamate and malate (**h**) and pyruvate and malate (**i**), but not alpha ketoglutarate and malate (**j**) or succinate (**k**), a complex II substrate.  $N = 9$  in the post vehicle and 8 in the post-corticosterone treatment group; two-sided  $t$ -test, \*\* $p = 0.0013$ , \*\*\*\* $p < 0.0001$ . **l** Complex I oxidized NADH at a significantly reduced rate in post-corticosterone EECs, indicating decreased complex I activity.  $N = 5$ ; two-sided  $t$ -test. \*\* $p = 0.0087$ . **m** Ndufa1 protein band volume relative to alpha-tubulin loading control band volume from EEC whole cell lysate. Processing of the blot is described in detail in.  $N = 3$  in the post-vehicle and 4 in the post-corticosterone treatment group; two-sided  $t$ -test, \* $p = 0.0364$ . For all, data are mean  $\pm$  SEM. For all appropriate, respirometry data is normalized by average  $\mu$ g protein/well from post-corticosterone or post-vehicle treatment wells without Mito Stress Test injections. The post-vehicle treatment group is represented by black or gray points or bars, post-corticosterone treatment group is represented by light blue. Source data are provided as a Source Data file. Figure 4a, f created with BioRender.com released under a Creative Commons Attribution-NonCommercial-NoDerivs 4.0 International license (<https://creativecommons.org/licenses/by-nc-nd/4.0/deed.en>).

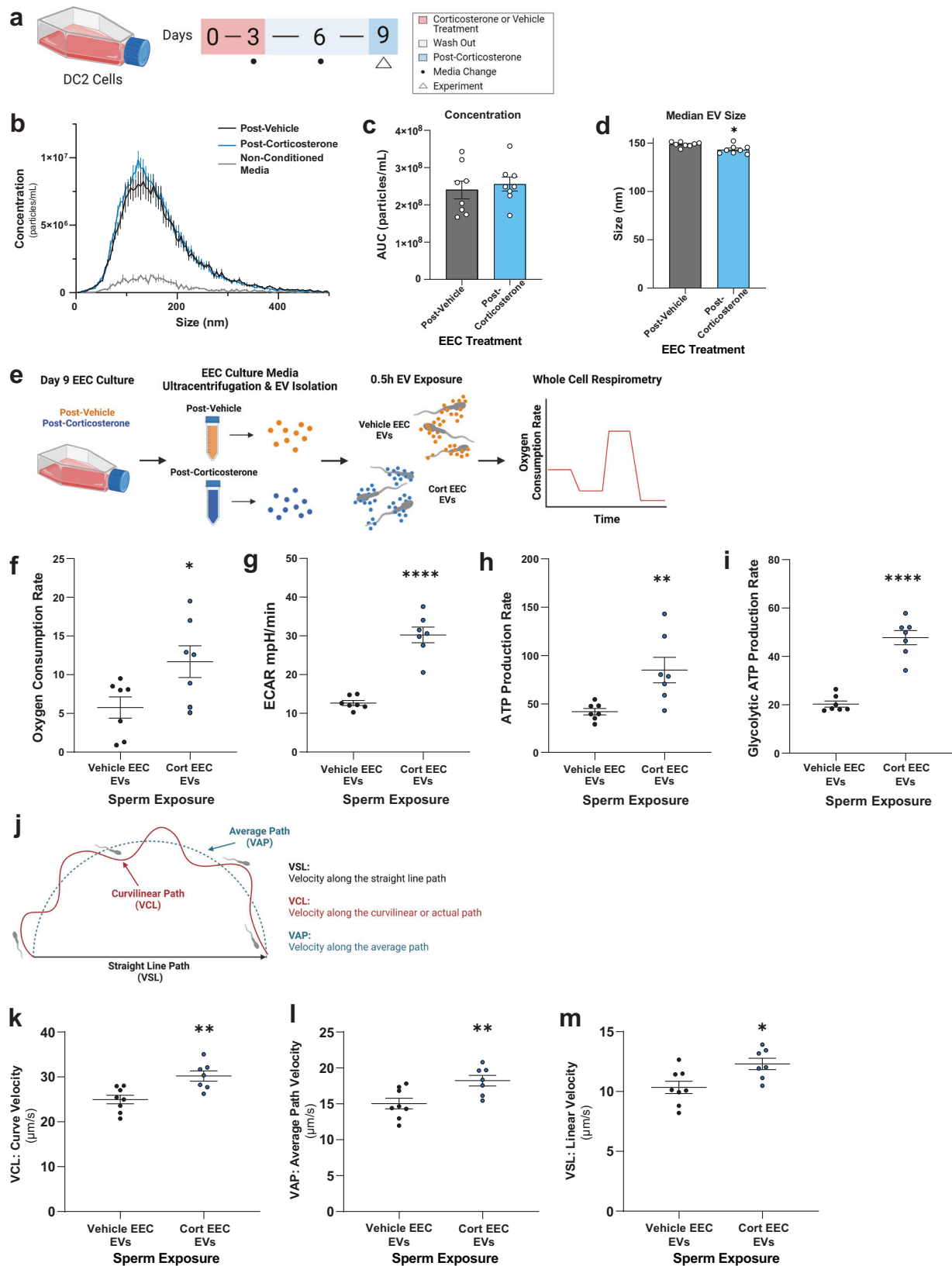
work reported that stress influenced chromatin accessibility, and H3K9ac and H3K79me3 distributions in other tissues, supporting chromatin reprogramming as a shared mechanism to recalibrate the cellular basal state following stress<sup>62,78,88,89</sup>.

As CUT&RUN revealed dramatic reprogramming of H3K27me3 distribution at loci important for metabolic and mitochondrial processes post treatment, and the majority of metabolic and mitochondrial genes were transcribed within the nucleus, we next examined the allostatic mitochondrial mechanisms involving the nuclear transcriptome. Weighted correlation network analysis (WGCNA) compared co-varying and differentially expressed genes over time following EEC corticosterone treatment. Of the eleven modules of co-varying gene sets, treatment strongly correlated with the module containing genes important for mitochondrial oxidative respiration and complex I assembly, identifying complex I as a molecular regulator of allostasis, likely engaged by prior corticosterone treatment across multiple cellular organelles. Taken together, these studies suggest changes in the cellular allostatic set point are characterized by a recalibration of mitochondria, particularly through regulation of complex I, and likely require a delicate integration of nuclear and mitochondrial regulatory processes<sup>39,90,91</sup>. Gene expression differences within group changed over time in culture, as expected, but these differences were distinct between groups. Hierarchical clustering analysis demonstrated that post-corticosterone and post-vehicle treatment groups cluster separately except for the day 9 post-corticosterone group that clustered between post-vehicle day 3 and day 6 groups, revealing differences in gene expression following treatment compared to the time-matched control at every timepoint. These results suggest that prior stress alters the trajectory of the transcriptome resulting in a gene expression profile reflective of an earlier state. In our assessment of gene expression at the latest timepoint post-treatment, 272 genes remained differentially expressed between time-matched groups. Interestingly, these changes persist at the same time as previously detected changes in EEC EV protein cargo<sup>25</sup>. Taken together with the WGCNA outcomes, these changes across time are indicative of a new allostatic state regulated in part at the level of the transcriptome. Further, over 68% of the EEC DEGs were *downregulated* following treatment, supporting the hypothesis that a common transcriptional regulatory mechanism, likely at the level of histone modifications including H3K27me3, has a lasting impact on the transcriptome.

To assess whether nuclear regulation of nuclear-encoded mitochondrial genes resulted in lasting changes in cellular energy requirements in our model, we utilized whole cell respirometry and detected significant deficits in basal mitochondrial respiration and oxidative ATP production rate. These results were further supported by transmission electron microscopy that revealed increased

orthodox mitochondrial ultrastructure following treatment, a phenotype associated with lower ADP levels (lower energy demand) and reduced respiration<sup>52,92,93</sup>. Importantly, there were no differences in total mitochondrial number or size, suggesting decreases in respiration were driven by mitochondrial processes and not the presence of fewer mitochondria. These findings indicated that at baseline, mitochondrial respiratory functions were decreased in post-corticosterone treated cells, supporting the hypothesis that treatment changed the energy required by basal cellular functions and therefore the mitochondrial energy production required to meet these demands. Recent studies examining the lasting effects of chronic stress at the cellular level in vivo reported similar reductions in mitochondrial respiration<sup>40,94–96</sup>. It is well established that allostatic regulation requires energy, is closely linked to oxidative and glycolytic processes at the mitochondria, and that as an allostatic regulator, corticosterone engages metabolic and mitochondrial processes<sup>10,12,37–40,64</sup>. Therefore, the lasting changes in mitochondrial respiration associated with dramatic reprogramming of a ubiquitous histone modification at the same timepoint further support a role for the mitochondria as a sensitive gauge for changes in the cellular allostatic state and reflects an integrated epigenetic and energetic adaptive mechanism. Together, these results demonstrated that changes in the metabolic state of the cell persist long after corticosterone treatment ended, a recognizable requirement of a new allostatic set point.

We next evaluated the potential contribution of the glucocorticoid receptor (GR) in mediating the decreased mitochondrial respiration detected following corticosterone treatment. We found increased levels of GR in the mitochondria enriched cellular fraction, and reduced levels in the nuclear enriched fraction compared to controls, suggesting a potential involvement of GR on the allostatic resetting of mitochondrial activity. Similarly, methods for both GR knockdown and GR antagonism rescued a hypo-respiratory mitochondrial phenotype, as expected<sup>97–101</sup>. Previous studies have also reported that in other tissues and cell types, such as the brain, GR translocated to the mitochondria immediately after glucocorticoid treatment and interacted with glucocorticoid response elements in the mitochondrial genome to acutely regulate transcription of complex I (*ND-1*) and III (*COX-1* and *COX-III*) subunits<sup>41,102–104</sup>. Alternatively, GR may also influence mitochondrial respiration by interacting directly at the electron transport chain or with co-regulatory proteins<sup>42,105</sup>. While GR influences mitochondrial outcomes including respiration and transcription, the change in mitochondrial function is cell-type and time-dependent<sup>41,42,103,104,106</sup>. Therefore, the immediate effects of glucocorticoid exposure differ from those following a period of recovery, further supporting the hypothesis that time is required following the end of stress for allostatic cellular reprogramming<sup>37,41,42,103,104</sup>.



As our model is uniquely positioned to examine a mitochondrial mechanism for the persistently decreased cellular respiration, we assessed glycolytic and oxidative respiratory processes in the EECs. We found prior corticosterone treatment decreased the oxidative, but not the glycolytic ATP production rate, and hypothesized that the allostatic set point was being regulated through oxidative respiration at

the electron transport chain independent of upstream glycolytic processes. As predicted, we found that respiratory deficits remained in the absence of substrates necessary for glycolysis, further implicating oxidative respiration as the source of hypo-respiration. At the electron transport chain, complex I is a primary regulator of oxidative ATP production, and is supplemented by complex II as the two entry points

**Fig. 5 | Prior stress exposed EEC secreted EVs increased sperm respiration and motility.** **a** Schematic of the timeline for the in vitro corticosterone treatment paradigm. The white arrow indicates when media was collected for ultra-centrifugation and EV isolation. **b** Plot of the size distribution of EVs isolated from day 9 EEC conditioned media.  $N = 8$ . **c** Area under the curve analysis (AUC) of the distribution confirmed there was no difference in EV concentration.  $N = 8$ . Student's  $t$ -test,  $p > 0.05$ . **d** Nanoparticle tracking analysis revealed post-corticosterone EEC EVs (cort-EEC EVs) had a decreased median size.  $N = 8$ . Two-sided  $t$ -test,  $*p = 0.0106$ . **e** Schematic detailing the protocol of conditioned media collection to EV isolation to sperm incubation and whole cell respirometry. **f** Baseline mitochondrial oxygen consumption rate.  $N = 7$  wells. Two-sided  $t$ -test,  $*p = 0.0334$ . **g** Extracellular acidification rate.  $N = 7$  wells. Two-sided  $t$ -test,  $****p < 0.0001$ . **h** ATP production rate.  $N = 7$  wells. Two-sided  $t$ -test,  $**p < 0.0081$ . **i** Glycolytic ATP production rate.  $N = 7$

wells. Two-sided  $t$ -test,  $****p < 0.0001$ . **j** Schematic detailing the CASA velocity outcomes following the EV incubation detailed in **e**. Curve velocity is red, average velocity is blue, and linear velocity is black. Increases in **k** curve velocity ( $**p < 0.0037$ ), **l** average velocity ( $**p < 0.0098$ ), and **m** linear velocity ( $*p < 0.0165$ ) as determined by CASA of all sperm analyzed. For **k–m**  $N = 8$  for vehicle and 7 for corticosterone EEC EV incubation groups; Two-sided  $t$ -test. For all panels, data are mean  $\pm$  SEM. For sperm respiratory data, average number of cells/well was used for normalization. The post-vehicle treatment group is represented by black or gray points or bars, post-corticosterone treatment group is represented by light blue. Source data are provided as a Source Data file. Figure 5a, e, j created with BioRender.com released under a Creative Commons Attribution-NonCommercial-NoDerivs 4.0 International license (<https://creativecommons.org/licenses/by-nc-nd/4.0/deed.en>).

for NADH and FADH, respectively<sup>107</sup>. We next tested the contributions of complex I and II in corticosterone treatment-dependent respiratory deficits by measuring the change in respiration following the addition of substrates for each. We found that the substrates for complex II, but not for complex I, increased the oxygen consumption rate in our cells. Importantly, we confirmed that prior corticosterone treatment reduced both complex I enzyme activity and levels of Ndufa1, a complex I subunit critical for assembly at the mitochondrial inner membrane<sup>53–56</sup>. These findings aligned with the earlier transcriptomic analyses that identified complex I as a key regulator of the allostatic set point following treatment. Therefore, these data support our hypothesis that allostatic mitochondrial adaptations are driven, at least in part, by significant decreases in complex I function. As previous studies reported similar mitochondrial respiratory phenotypes in animal models with prior stress exposure, the current data contribute a likely common mitochondrial mechanism of allostasis across tissues<sup>63</sup>.

We and others have focused on a key outcome of cellular allostasis involving the coordination of local and systemic cellular signaling by extracellular vesicles (EVs), biological nanoparticles secreted by cells to allow rapid and dynamic intercellular communication and coordination<sup>25,108–110</sup>. In the case of EECs, EV secretion into the caput lumen is a necessary process for sperm maturation<sup>17,20,24–26,33,36,111</sup>. Further, we previously showed in vitro and in vivo that prior stress treatment significantly altered EV size and cargo, including protein and sncRNA, and that incubation of sperm with these EVs significantly impacted embryo and fetal development<sup>25,34</sup>. Therefore, given the profound and persistent changes in transcriptomic, epigenetic, and metabolic and mitochondrial processes in EEC allostasis we had identified, we utilized our model to next test whether these EVs communicate regarding a metabolic state. In fact, we found that treatment-naïve EECs incubated with EVs secreted by post-corticosterone cells recapitulated the hypo-respiratory mitochondrial phenotype. This supports an important EV capability to facilitate functional changes in key cellular metabolic processes. Therefore, we next tested the ability for secreted EEC EVs to acutely regulate sperm mitochondrial respiration by incubating sperm with EVs and examining mitochondrial respiration by whole cell respirometry. Indeed, we found that EVs secreted post-corticosterone treatment (cort EEC EVs) significantly increased sperm oxygen consumption and ATP production rate, providing evidence that EVs secreted by EECs in an allostatic state causally and dynamically change sperm energy requirements. While the specific type of EV or its cargo involved in this communication are not known at this time, our data revealing increased extracellular acidification and glycolytic ATP production rates suggest EVs could have influenced respiration by regulating sperm glycolytic processes in alignment with prior studies<sup>112</sup>.

Importantly, the distinction between the *increased* sperm mitochondrial respiration and the *decreased* EEC respiration is that the latter is a direct effect of corticosterone reprogramming the somatic EEC allostatic state in the time *following* stress. The effect on sperm is

indirect, where a change in sperm function follows a change in the EVs produced by EECs at a new allostatic set point. This distinction is also key to understanding differences in the metabolic outcomes in EECs compared to sperm, as these data reveal that the EEC allostatic state is driven at the level of oxidative mechanisms, while sperm respirometry data support a change in glycolytic energy production driven by EV signaling. Furthermore, the unique mechanisms and timing underlying EV interactions with different cell types are not known, and the transient impact of EVs on EECs may differ from the observed long-term hypo-respiratory phenotype. However, these data indicate there may be unique downstream effects when EVs interact with germ cells relative to somatic EECs.

Ultimately, validating the functional relevance of sperm respiratory changes is key to contextualizing its biological importance. For sperm, motility is a direct readout of mitochondrial respirometry<sup>113–115</sup>. Therefore, we next utilized Computer Assisted Sperm Analysis (CASA) to determine if in the same timeframe in which EVs conferred significant changes on sperm respiration, we could detect differences in motility. Similar to our EV effects that increased sperm ATP production, prior corticosterone treatment produced EVs that when incubated with sperm significantly increased sperm motility, including VCL, VAP, and VSL. Interestingly, this effect persists despite methodological factors such as EV incubation time that may influence motility. Though the overall timing differs between the in vitro model and our human cohort, utilizing a model of allostasis we reveal similar outcomes in sperm motility and identify EEC EVs as critical intercellular communicators of organismal metabolic state capable of significantly altering sperm function. Finally, while the current study did not assess sperm fertility, our previous studies demonstrated that this same sperm-EV incubation in mice causally regulated fetal development and reproduced paternal stress phenotypic outcomes, signifying that these early changes in sperm metabolic state likely have important implications for the resulting embryos<sup>25,116–119</sup>. Fertility is a multifaceted process influenced by a host of maternal and paternal factors likely including EV communication. Our recently published study examining the longevity of epididymal EVs in the reproductive tract and post-fertilization processes using a novel CD63 tag revealed that EEC cargo are transferred to fertilized embryos following artificial insemination and still detectable at the embryo stage of development<sup>34</sup>. Therefore, these results suggest that though washing and isolating sperm from ejaculate is the gold standard in fertility medicine<sup>120</sup>, such protocols may be eliminating signals, including EVs, important for as-of-yet unidentified reproductive outcomes.

Overall, our findings from a healthy human cohort revealed a significant positive association between prior PSS and sperm motility outcomes that may be important for reproductive health<sup>2,80–82</sup>. The timing of this effect at 2–3 months following high PSS replicated our prior work examining sncRNA changes in sperm and points to similar cellular signaling mechanisms at work<sup>30</sup>. Utilizing an established cellular stress model, we identified the molecular processes important for allostasis, including the specific and significant resulting

mitochondrial and epigenetic changes that take place following stress. Ultimately, cellular communication with sperm by secreted EVs demonstrated significant effects on sperm respiration resulting in increased sperm motility. Taken together, these translational studies revealed a conserved, time-dependent association between prior perceived stress and essential sperm functions driven by allostatic mechanisms and identified EVs as critical intercellular communicators with potential therapeutic applications.

## Methods

### Recruitment of human subjects

The study was approved by the Colorado Multiple Institutional Review Board at the University of Colorado, all participants were English-speaking, provided written informed consent, and were compensated for their participation at each visit. A cohort of 34 healthy males were recruited from the University of Colorado and Denver Metropolitan area. Participants were recruited using social media including Reddit, Instagram, and Snapchat, fliers (University of Colorado Anschutz Medical Campus and Denver Campus, University of Denver, and Rocky Vista University), and University of Colorado Anschutz Medical Campus listservs. Subjects between the ages of 18 and 35 were screened for history of major medical illnesses, mental health diagnoses, and substance abuse. Key exclusion criteria included: 1) history of medical major medical illnesses such as known malignancy, sexually transmitted illness diagnosed within the last six months, history of stroke or other medical conditions deemed that the physician investigator deemed as contraindicated for the participant to be in the study as determined by participant self-report, 2) use of psychotropic (e.g. antidepressant or anxiolytic) medications within the last year or use of steroidal or beta blocker medications, 3) known sperm abnormalities, infertility, or testicular injury or disease, 4) extreme physical activity that may affect sperm, 5) psychiatric diagnosis in the previous year or lifetime diagnosis of psychotic disorder, 6) substance use disorder in the past year, current daily use of nicotine or cannabis products, or heavy drinking per National Survey of Drug Use and Health criteria, 7) three or more study visits with an average total motile count <5 million motile sperm, 8) body mass index >30. Participants with a score of greater than one on the Adverse Childhood Experiences (ACE) questionnaire were excluded from analyses<sup>50</sup>. The cohort currently consists of  $N=34$  participants across 146 observations, and for PSS Time -1 analyses compared  $N=34$  participants across 145 observations due to a missed visit.

### Study procedures for human subjects

The study involved a pre-screening survey and up to 9 visits. The pre-screening survey assessed basic study eligibility criteria. The first visit was a screening visit to determine eligibility, complete the informed consent processes, review the Adverse Childhood Experiences (ACE) questionnaire<sup>121</sup> for accuracy, administer the Mini International Neuropsychiatric Interview (MINI)<sup>122</sup> and urine drug screen. For healthy, eligible participants as determined by criteria described above, assessments including demographics, and the Perceived Stress Scale<sup>123</sup> were administered. During visits 2-3 the PSS and urine drug screen was readministered. The first three visits allow for a record of PSS for up to three months prior to the first semen collection. Visits 4-9 were identical to visits 2-3 with the addition of a fresh semen collection. The sample collection could be performed at home if the participant lived within 30 minutes of the study site, and any participant could elect to collect their semen sample at the study site at the time of the follow-up visit. Participants were required to remain abstinent for at least two days prior to the sample collection. Time and location of ejaculation were recorded. Samples were received at the lab within an hour of ejaculation and processed following the WHO recommendations for the examination and processing of human semen<sup>124</sup>. Briefly, samples were liquefied at 37 °C

for 30 minutes, visualized by wet mount, vortexed and 50  $\mu\text{L}$  was aliquoted for Computer Assisted Sperm Analysis.

### Human computer assisted sperm analysis

Aliquots were kept at 37 °C before loading 5  $\mu\text{L}$  into a prewarmed 20  $\mu\text{m}$  chamber slide (CellVision, CV 1020-2CH) and analyzing sperm motility using the Sperm Class Analyzer (Microoptics SL) system described above. Six randomly selected microscopic fields were captured (25 frames/second; 25 images per field) and analyzed by the software using standard parameters for human semen analysis including those identifying immotile (<5  $\mu\text{m/s}$ ), slow-medium (>5  $\mu\text{m/s}$ ), and rapid (>25  $\mu\text{m/s}$ ), with progressive sperm defined by  $\text{STR} > 80$ . Curvilinear velocity (VCL), straight-line velocity (VSL), and average path velocity (VAP) were measured.

### Mixed-effects modeling

To model the association of human sperm velocity and prior perceived stress, data were analyzed by random intercept mixed-effects (ME) modeling using the *nlme* (version 3.1-162)<sup>125,126</sup> and *effects* (version 4.2-2)<sup>127,128</sup> packages. This hierarchical modeling techniques accounted for the nested data structure (Level 1: Sample, Level 2: Participant, with 1 to 6 samples within any participant), and independent models analyzed all samples for each velocity parameter at each prior perceived stress time. In all cases modeling sperm velocity parameters (curve velocity, average path velocity, and straight-line velocity) and prior perceived stress at various time points, log transformation of the velocity parameter generated the best fit model. Covariates for all ME models included days of abstinence, age, and the location of the collection as samples collected at participants' homes were noted to be received by the lab later than samples collected on at the study site.

### Cell culture

Immortalized mouse distal caput epididymal epithelial (DC2) cells purchased from Applied Biological Materials (TO599) and cultured as previously described<sup>129</sup>. Briefly, plates were coated with collagen type 1, rat tail (Millipore, C3867), cells were plated at equal density, and cultured in IMDM (Gibco, 12440061) with 10% FBS (Gibco, 26140079) and 1% penicillin-streptomycin (Gibco, 15070063). Media was replaced at monolayer confluency at day 0, and cells were treated with 1:1000 vehicle (0.1% ethanol) or 1:1000 corticosterone in ethanol (Cayman Chemical, 16063; 500 ng/ml corticosterone). Media was replaced 72 hours, and 144 h later. For collection, cells at an average confluency of 0.65 million cells/cm<sup>2</sup> by day 9 were trypsinized in 0.25% trypsin-EDTA (Gibco).

### Animals

All studies were performed according to experimental protocols approved by the University of Maryland or the University of Colorado Institutional Animal Care and Use Committee, and all procedures were conducted in accordance with the NIH Guide for the Care and Use of Laboratory Animals. Male C57BL/6J and female 129S1/SvImJ mice were obtained from Jackson Laboratories to produce C57BL/6:129 hybrids. Hybrid males were 14-15 weeks of age at the time of sperm collection for all experiments. All mice were housed in a 12:12 light:dark cycle with temperature 22 °C and relative humidity 37%. Food (Teklad 2920X irradiated rodent diet) and water were provided ad libitum.

### Tissue collection and sperm EV incubation

Sires were decapitated under isoflurane anesthesia. M2 media (Sigma, M7167) supplemented with 1 mM ZnCl (Sigma, Z0152) and equilibrated to 5% CO<sub>2</sub> at 37 °C (pH=6.7) in a droplet contained in mineral oil (Sigma, M5904). For each experiment, four total caudal epididymis were removed from two males, minced in the supplemented M2 media droplet, and incubated at 37 °C, 5% CO<sub>2</sub> for 0.75 h to allow for sperm to swim out. Sperm were collected from the droplets, pooled, counted,

centrifuged for 2 minutes at 400 xg, and resuspended in supplemented M2 media at  $2 \times 10^9$  EVs/million sperm. 12 million sperm were allocated per group in respirometry experiments, and 8 million sperm per group in motility studies. Sperm-EV incubations lasted 0.5 h before centrifugation at 400 xg for 3 minutes. Sperm were resuspended as described below for downstream experiments.

### Cleavage Under Targets and Release Using Nuclease (CUT&RUN)

The CUT&RUN protocol was adopted from the Nature Protocols manuscript by Skene, Henikoff & Henikoff<sup>130,131</sup>. 500k EECs were collected for each antibody incubation (anti-H3K27me3 antibody, Sigma, 07-499; anti-Rabbit IgG, Antibodies Online, ABIN101961). An anti-Rabbit IgG antibody was utilized as a negative control to assess non-specific binding. Cells were bound to concanavalin-A coated beads (Bangs Labs, BP531) and incubated with antibody overnight. pA/G MNase fusion protein (Cell Signaling, 40366S) was bound during a 1 h incubation at 4 °C and activated with 2 mM CaCl<sub>2</sub> during a 0.5 h incubation at 0 °C. Samples were incubated at 37 °C for 0.5 h to release chromatin fragments into the supernatant. Supernatant was collected and DNA was extracted using phenol:chloroform:isoamyl alcohol. DNA concentration was determined using the High Sensitivity dsDNA Qubit Assay (Invitrogen, Q32851) and fragment sizes were determined using the High Sensitivity D1000 ScreenTape Assay (Agilent, 5067-5584 and 5067-5585). DNA libraries were prepared using the NEBNext Ultra II DNA Library Prep Kit for Illumina (NEB, E7645) with the NEBNext Multiplex Oligos for Illumina (Dual Index Primers Set I) (NEB, E7600S). All library sizes and concentrations were confirmed on a TapeStation 4200 (Agilent) and Qubit 3.0 Fluorometer (Thermo Fisher). Individually barcoded libraries were pooled and sequenced on an Illumina NextSeq 500 (75-bp paired-end).

### RNA isolation

Total RNA extraction from DC2 cell pellets was done using the TRIzol reagent (Thermo Fisher, 15596026) according to manufacturer's protocol.

### mRNA sequencing

Total RNA from DC2 cell pellets were quantified on a NanoDrop 2000 spectrophotometer (Thermo Scientific). Libraries for RNA-seq were made using a TruSeq Stranded mRNA Sample Preparation Kit (Illumina) with 500 ng RNA. All library sizes and concentrations were confirmed on a TapeStation 4200 (Agilent) and Qubit 3.0 Fluorometer (Thermo Fisher). Individually barcoded libraries were pooled and sequenced on an Illumina NextSeq 500 (75-bp single-end). FASTQ files were processed for pseudoalignment and abundance quantification of reads to the *Mus musculus* reference transcriptome (version 38) using Kallisto<sup>132,133</sup>.

### Lentiviral particle transduction and shRNA knockdown confirmation by RT-qPCR

At 80% confluency, DC2 cells were exposed to 18,000 transducing units of viral particles in culture media containing 8 µg/mL hexadimethrine bromide. Cultures were incubated with particles overnight. MISSION TRC2 pLKO.5-puro Empty Vector Control Transduction Particles (Sigma, SHC201V) (Empty Vector) collected for the transduction, MISSION TRC2 pLKO.5-puro Non-Mammalian shRNA Control Transduction Particles (Sigma, SHC216V) controlled for shRNA expression, and MISSION shRNA Lentiviral Clone Oligo TRCN0000026223 (Sigma, SHCLNV) expressed shRNA to knockdown GR. Media was exchanged after the overnight incubation, and then into selection media containing 2 µg/mL puromycin (Sigma-Aldrich, P9620) after 24 hours. After 12 days, cells were passaged for colony selection using the agarose method (<http://thelindberglab.com/cloning-cells-with-the-agarose-method/>). Colonies were maintained and passaged as necessary in selection media until they were cryopreserved. For experiments,

cultures were maintained in selection media throughout experiments resulting in GR knockdown across all experimental timepoints.

GR (*Nr3c1*) mRNA knockdown was confirmed by isolating RNA, and then synthesizing cDNA using the High Capacity cDNA Reverse Transcription Kit (Applied Biosystems, 4368814) according to the manufacturer's protocol. Reverse-transcription quantitative real-time PCR (RT-qPCR) quantified expression in conjunction with TaqMan Assays (Applied Biosystems, 4444556) according to the manufacturer's protocol. Briefly, each reaction was run in triplicate and samples were probed for *Nr3c1* (ThermoFisher Scientific, Assay ID: Mm00433832\_m1, Catalog #4331182) and endogenous 18S rRNA control (Applied Biosystems, 4332641). Reactions were run on a QuantStudio 5 Real-Time PCR System, and Ct values were calculated using the instrument's software. Mean Ct values for the endogenous control were subtracted from the Ct values of *Nr3c1*. These  $\Delta$ Ct values were used to calculate expression relative to the non-targeted shRNA control using the  $\Delta\Delta$ Ct method.

### Respirometry

Respiration reported as oxygen consumption rates (OCR) were measured in intact adherent DC2 cells with a Seahorse Extracellular Flux (XF96) Analyzer (Agilent). Cells were seeded at 3 million cells/well in Seahorse XF96 Microplates (Agilent, 101085-004) and treated as described before performing respirometry. Medium was replaced with Seahorse XF Base Medium (Agilent) supplemented with 15 mM glucose (Gibco, A2494001), 1 mM sodium pyruvate (Gibco, 11360070), and 4 mM L-glutamine (Gibco, 25030081), pH 7.4, unless indicated otherwise and incubated in a non-CO<sub>2</sub> incubator at 37 °C for less than one hour. Cells were washed within 1 h before taking measurements. The XF96 FluxPak (Agilent, 102416-100) cartridge was hydrated in water overnight before calibrating with Seahorse XF Calibrant Solution (Agilent, 103681-100). For the Mito Stress Test (Agilent, 103015-100), the cartridge was loaded per manufacturer's instructions with final concentrations of 1.5 µM oligomycin, 2 µM trifluoromethoxy carbonylcyanide phenylhydrazone (FCCP), and 0.5 µM Rotenone/Antimycin A (Agilent) after injection. For intact cells with additional injections, 10X solutions of sodium pyruvate (Gibco, 11360070) and L-glutamine (Gibco, 25030081) were prepared in respiration media before loading. In all DC2 cells, the injection protocol required 3 min mix, 0 min wait, and 3 min measure for 3 cycles per injection.

To incubate DC2 cells with EV, the above protocol was followed with the exception that at the indicated times culture medium was supplemented with  $3.14 \times 10^8$  EVs/mL in PBS, or an equal volume of PBS control for 3 days. After EV exposure, media was replaced with respirometry media and assayed as described above.

For experiments requiring permeabilization of DC2 cells during analyzer measurements, respiration was measured in a low potassium, low calcium buffer (3.5 mM KCl, 120 mM NaCl, 0.4 mM KH<sub>2</sub>PO<sub>4</sub>, 1.2 mM Na<sub>2</sub>SO<sub>4</sub>, 2 mM MgCl<sub>2</sub>, 20 mM Na-N-Tris-(hydroxymethyl)-methyl-2-amino-ethanesulfonic acid (TES pH 7.4), 1 mM EGTA, 0.4% wt/volume fat-free bovine serum albumin (BSA)). 10X solutions of recombinant perfringolysin O (rPFO) and substrate combinations (malic acid with alpha-ketoglutarate, sodium pyruvate, or L-glutamic acid, and succinic acid) were prepared in the same buffer with final diluted concentrations of 5 nM rPFO, and 10 mM substrate<sup>134</sup>. For permeabilization, the injection protocol required 0.5 min mix, 1 minute wait, 3 min measure for 3 cycles per baseline or injection.

Following respirometry, wells which had no injections were washed twice with cold PBS before lysing with RIPA Lysis Buffer prepared in cold PBS with cOmplete, EDTA-free protease inhibitor (Roche, 11697498001) for 5 minutes. Protein concentration for normalization was quantified from these wells using the Pierce BCA Protein Assay Kit (Thermo Scientific, 23227) and analyzed on an Infinite M1000 plate reader (Tecan) using Magellan software (Tecan).

Protein was averaged across the wells in each group for normalization.

To measure respiration in sperm, Seahorse microplates were coated with 0.5 mg/mL concanavalin A (Sigma, C5275) in PBS for 1 hour before removing the coating and allowing the plate to dry overnight at room temperature as previously reported<sup>135</sup>. Mito Stress Test reagents were loaded into the cartridge in sperm respiratory media (Seahorse XF Base Media supplemented with 5.6 mM glucose, 1 mM pyruvate, 2 mL glutamine, 3 mg/mL fat free BSA, pH 6.9), at the concentrations above, except that the final concentration of FCCP was determined to be 1  $\mu$ M. Following 0.5 h EV incubation at the same concentration as above, sperm were resuspended 1 million sperm per 50  $\mu$ L sperm respiratory media, plated 1 million sperm/well, and centrifuged at 250  $\times$  g for 1 minute before adding media to 200  $\mu$ L/well. Sperm were visualized using a light microscope to ensure even distribution prior to plate loading. Respiration was measured following a 1-minute mix and 2-minute measure cycles protocol<sup>135</sup>. Three cycles were recorded for each step. Total cell count/well was used for normalization.

Respiration calculations following the Mito Stress Test were performed following previously published recommendations by the manufacturer and others<sup>51,136,137</sup>. In assays requiring permeabilization with rPFO the difference in OCR (dOCR) between peak respiration following substrate addition and the minimum respiration following permeabilization was calculated.

### Complex I Enzyme Activity

Activity was measured in black walled, transparent bottom plates following the Complex I Enzyme Activity Microplate Assay Kit (Abcam, ab109721) manufacturer's protocol on an Infinite M1000 plate reader (Tecan) and analyzed using Magellan software (Tecan). Protein concentration for normalization was quantified by Pierce BCA Protein Assay Kit (Thermo Scientific, 23227).

### Mitochondria isolation and protein extraction

Mitochondria were isolated from EECs using a previously described protocol<sup>138</sup>. Half of the sample was used for this protocol and half were pelleted and snap-frozen for nuclear extraction described below. Briefly, for mitochondria isolation, cells were resuspended in an equal volume ice-cold hypotonic buffer (10 mM NaCl, 1.5 mM MgCl<sub>2</sub>, 10 mM HEPES, pH 7.5) and allowed to swell for 10 minutes. Cells were homogenized on ice using 20 strokes of the dounce homogenizer B pestle to produce greater than 50% lysed cells. 5X extraction buffer (50 mM HEPES pH 7.5, 1 M mannitol, 350 mM sucrose, 5 mM EGTA) was added with a final 1X concentration and one stroke was performed with the dounce homogenizer. The homogenate was centrifuged twice at 4  $^{\circ}$ C, 1300  $\times$  g for 5 minutes. The supernatant was centrifuged at 4  $^{\circ}$ C at 17000  $\times$  g for 15 minutes resulting in the mitochondrial pellet which was resuspended in 1 mL 1X extraction buffer before repeating the 15-min centrifugation. The final mitochondrial pellet was snap-frozen in liquid nitrogen and stored at  $-80^{\circ}$ C. Samples were thawed on ice for protein extraction with ice-cold RIPA lysis described above. Mitochondrial pellets were resuspended in 150  $\mu$ L cold lysis buffer, vortexed, incubated on ice for 5 minutes, and centrifuged at 8000 $\times$ g, 4  $^{\circ}$ C for 10 minutes to pellet debris. The supernatant was collected, and protein was quantified using the Pierce BCA Protein Assay Kit (Thermo Scientific, 23227) before storing at  $-80^{\circ}$ C.

### Nuclear isolation and protein extraction

Isolation of nuclei were performed using the Nuclei EZ Prep Kit (Sigma, NUC101) following manufacturer's protocol. Briefly, DC2 EEC pellets were thawed on ice, resuspended in 2 mL cold Nuclei EZ lysis buffer and incubated for 5 minutes on ice. 1.5 mL was homogenized using 5 strokes of the Dounce homogenizer pestle B on ice. The homogenizer was rinsed with 500  $\mu$ L of the Nuclei EZ lysis buffer which was added to the sample before centrifuging for 5 minutes at 500  $\times$  g, 4  $^{\circ}$ C.

The pellet was washed with 1 mL Nuclei EZ lysis buffer before 5-min centrifugation at 500  $\times$  g, 4  $^{\circ}$ C, and the wash was repeated. For protein extraction, the final pellet was resuspended in 200  $\mu$ L RIPA lysis buffer, prepared as above, shaken at 3000 rpm on the Disrupter Genie (Scientific Industries) for 15 minutes, 4  $^{\circ}$ C, and centrifuged 10 minutes at 1600  $\times$  g, 4  $^{\circ}$ C. The supernatant was collected, and protein was quantified and stored as above.

### Whole cell lysate protein extraction

EEC cell pellets were thawed on ice and resuspended in 2 mL RIPA buffer prepared as described above. The mixture was rotated end over end for 15 minutes at 4  $^{\circ}$ C, and centrifuged 15 minutes at 14,000  $\times$  g, 4  $^{\circ}$ C. The supernatant was collected, and protein was quantified as above.

### Western immunoblotting

For mitochondrial and nuclear protein, 20  $\mu$ g protein per lane was denatured by heating at 95  $^{\circ}$ C for 5 minutes before loading onto a NuPAGE 4-12% Bis-Tris pre-cast gel (Invitrogen, NP0335BOX) for gel electrophoresis. NuPAGE antioxidant (Invitrogen, NPO005) was added to the NuPAGE Running Buffer (Invitrogen, NPO002) prior to electrophoresis at 180 V for 50 minutes at room temperature. PVDF membranes (Millipore, IPFL07810) were activated in methanol for 30 s and rinsed in transfer buffer (Invitrogen, NP00061). Protein was transferred at 35 V for 60 minutes at 4  $^{\circ}$ C. The membrane was rinsed with water and blocked (Licor, 927-60001) for 1 hour at room temperature. Membranes were incubated overnight at 4  $^{\circ}$ C in Intercept Blocking Buffer with 0.1% Tween-20 and primary antibodies that included either anti-H3 antibody at 1  $\mu$ g/mL (Abcam, ab176842), anti-GR antibody at 1:500 dilution (Santa Cruz, sc393434X), or anti-ATP-5a antibody at 1:2000 dilution (Abcam, ab14748). For blots with >1 antibodies of the same species, the membrane was cut and incubated individually. Membranes were rinsed with PBS with 0.1% Tween-20 and incubated with the appropriate secondary antibodies including either IRDye 800CW Donkey anti-Mouse IgG secondary antibody at 1:5000 dilution (Licor, 926-32212) or IRDye 680RD Donkey anti-Rabbit IgG secondary antibody at 1:5000 dilution (Licor, 926-68073).

For whole cell lysate protein probed for Ndufa1, the same procedures were followed with the following exceptions. 16  $\mu$ g protein was loaded per well on a NuPAGE 12% Tris-Bis pre-cast gel. The gel was cut prior to transfer to ensure optimal transfer of proteins of differing sizes. Protein was transferred to a nitrocellulose membrane (Invitrogen, LC2000) with the upper portion transferring for 40 minutes at 30 V, then 20 minutes at 35 V, and while the bottom transferred for 40 minutes at 30 V, both at 4  $^{\circ}$ C. Each membrane was probed with either anti-alpha tubulin primary antibody at 1:1000 dilution (Sigma, T5168) or anti-Ndufa1 at 1:1000 (MWFE) primary antibody (generously donated by Dr. Nagendra Yadava) for 1 h at room temperature<sup>139-141</sup>. Following washes, membranes were incubated for 1 h at room temperature with either IRDye 680RD Donkey anti-Mouse IgG secondary antibody at 1:2000 dilution (Licor, 926-68072) or IRDye 800CW Donkey anti-Rabbit IgG secondary antibody at 1:3000 dilution (Licor, 926-32213).

### Transmission electron imaging (TEM)

DC2 cultures were washed with PBS and fixed overnight in a solution of 2% paraformaldehyde, 2.5% glutaraldehyde in 0.1 M PIPES buffer (pH 7.2) for an hour at room temperature and then left overnight at 4  $^{\circ}$ C. After fixation, cells were washed in PIPES buffer, quenched in 50 mM glycine in 0.1 M PIPES buffer for 15 minutes, scraped off the plate and collected by centrifugation. Cell pellets were enrobed in 2.5% low melting point agarose, trimmed into 1 mm<sup>3</sup> blocks and post-fixed with 1% osmium tetroxide, 0.25% potassium ferrocyanide in 0.1 M PIPES buffer for 1 hour on ice. After washing, agarose blocks were loaded in the mPrepS capsule, block stained with 1% Uranyl acetate, dehydrated,

and infiltrated in Araldite resin in an automated specimen processor ASP-1000 (Microscopy Innovations). Samples were embedded in pure Araldite resin and polymerized at 60 °C for 24–48 hours. Ultrathin sections at ~70 nm thickness were cut on a Leica UC6 ultramicrotome (Leica Microsystems) and examined in a FEI Tecnai T12 electron microscope operated at 80 kV. Digital images were acquired by using an AMT bottom mount CCD camera and AMT600 software. Mitochondria in micrographs taken at 6500x magnification were identified and analyzed in ImageJ using methods described previously<sup>142</sup>.

### Extracellular vesicle isolation

EVs were harvested from cultures in medium supplemented with EV-depleted FBS (System Biosciences, EXO-FBS-50A-1)<sup>143,144</sup>. EVs were isolated by differential ultracentrifugation from conditioned media collected 72 hours after the last media change at day 9. Debris was removed by centrifugation at 2000 × g for 10 minutes at 4 °C in a A-4-44 swing-bucket rotor (Eppendorf) followed by 9000 rpm (avg 10,000 × g) for 35 minutes at 4 °C using the Beckman Coulter LE-80 Ultracentrifuge and SW 32 Ti Swinging-Bucket Rotor (Beckman Coulter), which was used for all remaining ultracentrifugation. EVs were pelleted by ultracentrifugation at 28,500 rpm (average 100,000 × g) for 100 minutes at 4 °C. Supernatant was aspirated and the pellet resuspended in 30 mL cold, filtered (0.22 μm) PBS. Ultracentrifugation at 28,500 rpm (avg 100,000 × g) for 100 minutes at 4 °C was repeated and the supernatant aspirated, leaving less than 1 mL PBS for resuspension, before freezing at -80 °C.

### Nanoparticle tracking analysis (NTA)

The concentration and size of EVs were measured using a ZetaView BASIC Nanoparticle Tracking Analysis Microscope (Particle Metrix). EVs were thawed on ice and diluted 1:500 in freshly filtered (0.22 μm) water to achieve ~200 particles per frame. 11 cell positions were scanned with 30 fpp over 2 cycles to acquire concentration, size, and charge data. Video acquisition sensitivity was 80 and shutter speed was 100. Videos were analyzed with the Native software (version 8.05.14). Minimum brightness was 20, minimum area was 10, and maximum area was 1000.

### Mouse computer assisted sperm analysis

Following 0.5 h EV incubation (as described above), sperm were resuspended in sperm respiratory media as described. As sperm are still maturing while in the caput, caudal sperm were utilized for motility and respirometry assays. Sperm were plated 1 million sperm/well and kept on a plate warmer at 37 °C before loading 2.5 μL into a prewarmed 20 μm chamber slide (CellVision, CV 1020-4CH) and analyzing sperm motility using the Sperm Class Analyzer (Microoptics SL). This system consists of a microscope (Eclipse E600, Nikon) with a 10× objective under negative phase contrast (Nikon), a camera (Basler, acA1300-200uc), and a PC with the analysis software (SCA Version 6.6.15). Six randomly selected fields were captured (50 frames/second; 25 images per field) and analyzed by the software identifying immotile (<50 μm/s), slow-medium (>50 μm/s), and rapid (>200 μm/s), with progressive sperm defined by STR > 50. Curvilinear velocity (VCL), straight-line velocity (VSL), and average path velocity (VAP) were measured.

### Statistics & reproducibility

In human cohort studies, investigators were blinded to participants' stress and demographic metrics. In vitro and animal studies, samples were randomized to treatment groups and the investigators were blinded to allocation during experiments and outcome assessment. Statistical analyses were performed using GraphPad Prism (version 9.5.0), except for next-generation sequencing analyses. Respirometry, complex I enzyme function, western blot, EV AUC and size, CASA, and TEM data were analyzed by two-way ANOVAs or Student's *t*-tests as

appropriate. Kruskal Wallis test was used to analyze total sperm count and total motile sperm count across visits due to non-normal residuals as determined by Shapiro Wilk test. Non-parametric tests were only utilized when non-normal residuals were determined by Shapiro-Wilk test. Mitochondrial ultrastructures were analyzed using the chi square test. When appropriate, Bonferroni's or Sidak's multiple comparisons, or Tukey test was used to explore main effects. Significance was set at  $p < 0.05$ . The DC2 RNA sequencing experiment used a 0.5 minimum log<sub>2</sub>-fold-change (lfc) cutoff and significance was determined by false discovery rate (FDR) of <0.05. For the WGCNA, gene ontology for Biological Processes with FDR < 0.01 were reported. For CUTNRUN sequencing analysis, differential binding was determined by FDR < 0.05 in the CUTNRUN sequencing experiment. Linear mixed effects analyses are described below. Outliers were identified using the Grubbs' Test. In Western Immunoblotting, lanes were only excluded from analysis if a bubble was present in the band of interest impeding quantification of the entire volume of the band, and such incidences are noted within the whole blot image submitted to the journal.

### Bioinformatics analyses

Analyses were performed using R version 4.2.2 and Bioconductor version 3.16.0. Additionally, data from CUTNRUN were visualized using the usegalaxy.org online platform<sup>145</sup>.

### CUT&RUN Differential Binding Analysis (DBA) and Gene Set Enrichment Analysis

Briefly, alignment and data processing was performed following the protocols detailed in Skene, Henikoff & Henikoff<sup>130</sup>. Paired-end reads from the FASTQ files were aligned using Bowtie2 (version 2.4.2) to the Genome Reference Consortium Mouse Build 38 and the iGenomes *Escherichia coli* strain K12, MG1655 Build 2001-10-15 (Illumina) to allow for calibration based on carry over *E. coli* DNA introduced with the pA/G MNase using the `py_sam_2_spikenormbg.py` script<sup>130,146,147</sup>. Peak calling was performed using the `py_peak_calling.py` script. Both normalization and peak calling scripts are available at <https://github.com/peteskene>. DBA was performed using the Bioconductor package Diff-Bind (version 2.15.1)<sup>148</sup>. Peaks must have been present in a minimum of 4 peaksets with `Score=DBA_SCORE_TMM_MINUS_FULL` set in `dba-count`, using `method=DBA_EDGER` in `dba.analyze`. Peaks with differential binding determined by FDR < 0.05 were retained. Bioconductor packages ChIPpeakAnno (version 3.32.0) and ChIPseeker (version 1.34.1) were used to perform peak annotation, generate bar and distance to transcription site plots<sup>149,150</sup>. Heatmaps of representative samples were generated using Galaxy web platform on the public server at usegalaxy.org to analyze the data with the `deeptools` toolkit<sup>145,151,152</sup>. Peaks were visualized in Supplementary Fig. 2 using the UCSC Genome Browser<sup>153,154</sup>.

Gene Set Enrichment Analysis of Gene Ontology was performed using the Bioconductor package clusterProfiler (version 4.6.2) function `gseGO` with a minimum and maximum size of each geneSet assigned as 100 and 500, respectively, and the *p*-value adjustment method set to "BH".

### DC2 differential expression analysis

Our RNA sequencing pipeline was designed using the DIY Transcriptomics framework<sup>155</sup>. Briefly, Bioconductor package `tximport` (version 1.26.1) collapsed gene isoforms to gene symbols<sup>156</sup>. Genes included in the analysis had >1 counts/million in at least 4 samples and gene expression distributions were normalized using Bioconductor package `edgeR` (version 3.40.1)<sup>157</sup>. All heatmaps are plotted as average Z scores/treatment group and arranged through hierarchical clustering. The R package `Stats` (version 4.2.2) was used for principal component analysis and to cluster co-regulated genes (`method="spearman"`, `method="complete"`). Heatmaps were generated using R package `pheatmap` (version 1.0.12). The `limma` Bioconductor package

(version 3.54.0) function `voom` was used for normalization<sup>158</sup>. `limma` was also used to test normalized counts for differential abundance. The heatmap of differentially expressed genes between day 9 vehicle and corticosterone groups was generated using the `heatmap.2` function of the R package `gplots` (version 3.1.3).

### WGCNA

Gene expression in the bulk RNAseq dataset were subjected to weighted co-expression network analysis using the WGCNA package (version 1.71)<sup>159–161</sup>. Briefly, `blockwiseModules` was used for network construction and module detection across all genes using the following directives. Network construction used Pearson correlation to calculate the signed co-expression similarity, and the adjacency matrix was calculated using a soft-thresholding power of 6. Co-expression module detection used a dynamic tree cut algorithm limited to a minimum module size of 30 genes and a cut height of 0.25 for module merging. The Pearson correlations were calculated to quantify associations between module eigengenes and the features exposure and time, and the function `corPvalueStudent` calculated the asymptotic *p*-value for the given correlations. The DAVID Bioinformatics Database (version DAVID 2021) was used for functional annotation analysis of the biological processes associated with genes contained in the module most highly correlated to exposure<sup>162,163</sup>.

### Reporting summary

Further information on research design is available in the Nature Portfolio Reporting Summary linked to this article.

### Data availability

Next-generation sequencing data generated in this study have been deposited in Gene Expression Omnibus under accession code [GSE234633](https://www.ncbi.nlm.nih.gov/geo/query/acc.cgi?acc=GSE234633). Other data generated in this study are provided in the Supplementary Information. Source data are provided with this paper.

### References

- Dai, C. et al. Advances in sperm analysis: techniques, discoveries and applications. *Nat. Rev. Urol.* **18**, 447–467 (2021).
- Tiegs, A. W., Landis, J., Garrido, N., Scott, R. T. Jr. & Hotaling, J. M. Total Motile Sperm Count Trend Over Time: Evaluation of Semen Analyses From 119,972 Men From Subfertile Couples. *Urology* **132**, 109–116 (2019).
- Montero-Marin, J. et al. Young People's Mental Health Changes, Risk, and Resilience During the COVID-19 Pandemic. *JAMA Netw. Open* **6**, e2335016 (2023).
- Miao, R., Liu, C., Zhang, J. & Jin, H. Impact of the COVID-19 pandemic on the mental health of children and adolescents: A systematic review and meta-analysis of longitudinal studies. *J. Affect. Disord.* **340**, 914–922 (2023).
- Branje, S. The impact of the COVID-19 pandemic on adolescent mental health across the world. *Curr. Opin. Psychol.* **53**, 101665 (2023).
- Cummings, J. R. et al. Challenges facing mental health systems arising from the COVID-19 pandemic: Evidence from 14 European and North American countries. *Health Policy* **136**, 104878 (2023).
- Ilacqua, A., Izzo, G., Emerenziani, G. P., Baldari, C. & Aversa, A. Lifestyle and fertility: the influence of stress and quality of life on male fertility. *Reprod. Biol. Endocrinol.* **16**, <https://doi.org/10.1186/s12958-018-0436-9> (2018).
- Kasman, A. M., Del Giudice, F. & Eisenberg, M. L. New insights to guide patient care: the bidirectional relationship between male infertility and male health. *Fertil. Steril.* **113**, 469–477 (2020).
- Sterling, P. & Eyer, J. In *Handbook of Life Stress, Cognition and Health* (eds Fisher, S. & Reason, J.) Ch. 34, 629–639 (John Wiley & Sons, 1988).
- McEwen, B. Allostatic and Allostatic Load Implications for Neuropsychopharmacology. *Neuropsychopharmacology* **22**, 108–124 (2000).
- McEwen, B. S. Seminars in medicine of the Beth Israel Deaconess Medical Center: Protective and damaging effects of stress mediators. *N. Engl. J. Med.* **338**, 171–179 (1998).
- McEwen, B. S. Protection and Damage from Acute and Chronic Stress: Allostatic and Allostatic Overload and Relevance to the Pathophysiology of Psychiatric Disorders. *Ann. N. Y. Acad. Sci.* **1032**, 1–7 (2004).
- McEwen, B. S. Allostatic and the Epigenetics of Brain and Body Health Over the Life Course. *JAMA Psychiatry* **74**, 551 (2017).
- McEwen, B. S. & Stellar, E. Stress and the Individual: Mechanisms Leading to Disease. *Arch. Intern. Med.* **153**, 2093–2101 (1993).
- Gervasi, M. G. & Visconti, P. E. Molecular changes and signaling events occurring in spermatozoa during epididymal maturation. *Andrology* **5**, 204–218 (2017).
- Tourzani, D. A. et al. Caput Ligation Renders Immature Mouse Sperm Motile and Capable to Undergo cAMP-Dependent Phosphorylation. *Int. J. Mol. Sci.* **22**, 10241 (2021).
- Conine, C. C., Sun, F., Song, L., Rivera-Pérez, J. A. & Rando, O. J. Small RNAs Gained during Epididymal Transit of Sperm Are Essential for Embryonic Development in Mice. *Dev. Cell* **46**, 470–480.e473 (2018).
- Sharma, U. et al. Biogenesis and function of tRNA fragments during sperm maturation and fertilization in mammals. *Science* **351**, 391–396 (2016).
- Sharma, U. et al. Small RNAs Are Trafficked from the Epididymis to Developing Mammalian Sperm. *Dev. Cell* **46**, 481–494.e486 (2018).
- Sullivan, R., Frenette, G. & Girouard, J. Epididymosomes are involved in the acquisition of new sperm proteins during epididymal transit. *Asian J. Androl.* **9**, 483–491 (2007).
- Qing, X. et al. Dysregulation of an X-linked primate-specific epididymal microRNA cluster in unexplained asthenozoospermia. *Oncotarget* **8**, 56839–56849 (2017).
- Jaiswal, B. S., Das, K., Saha, S., Dungdung, S. R. & Majumder, G. C. Purification and characterization of a motility initiating protein from caprine epididymal plasma. *J. Cell. Physiol.* **222**, 254–263 (2010).
- Murta, D. et al. Notch signaling in the epididymal epithelium regulates sperm motility and is transferred at a distance within epididymosomes. *Andrology* **4**, 314–327 (2016).
- Rowlison, T., Ottinger, M. A. & Comizzoli, P. Exposure to epididymal extracellular vesicles enhances immature sperm function and sustains vitality of cryopreserved spermatozoa in the domestic cat model. *J. Assist. Reprod. Genet.* **38**, 2061–2071 (2021).
- Chan, J. C. et al. Reproductive tract extracellular vesicles are sufficient to transmit intergenerational stress and program neurodevelopment. *Nat. Commun.* **11**, 1499–1499 (2020).
- Rejraji, H. et al. Lipid remodeling of murine epididymosomes and spermatozoa during epididymal maturation. *Biol. Reprod.* **74**, 1104–1113 (2006).
- Nixon, B. et al. The MicroRNA Signature of Mouse Spermatozoa Is Substantially Modified During Epididymal Maturation. *Biol. Reprod.* **93**, 91 (2015).
- Frenette, G., Lessard, C. & Sullivan, R. Selected Proteins of "Prostasome-Like Particles" from Epididymal Cauda Fluid Are Transferred to Epididymal Caput Spermatozoa in Bull1. *Biol. Reprod.* **67**, 308–313 (2002).
- Sullivan, R. & Saez, F. Epididymosomes, prostasomes, and liposomes: their roles in mammalian male reproductive physiology. *REPRODUCTION* **146**, R21–R35 (2013).

30. Rimmer, M. P., Gregory, C. D. & Mitchell, R. T. The transformative impact of extracellular vesicles on developing sperm. *Reprod. Fertil.* **2**, R51–R66 (2021).
31. Reilly, J. N. et al. Characterisation of mouse epididymosomes reveals a complex profile of microRNAs and a potential mechanism for modification of the sperm epigenome. *Sci. Rep.* **6**, 31794 (2016).
32. Zhou, W. et al. Mechanisms of tethering and cargo transfer during epididymosome-sperm interactions. *BMC Biol.* **17** <https://doi.org/10.1186/s12915-019-0653-5> (2019).
33. Trigg, N. A., Eamens, A. L. & Nixon, B. The contribution of epididymosomes to the sperm small RNA profile. *Reproduction* **157**, R209–R223 (2019).
34. Morgan, C. P., Meadows, V. E., Marx-Rattner, R., Cisse, Y. M. & Bale, T. L. (2023) HA-tag CD63 is a novel conditional transgenic approach to track extracellular vesicle interactions with sperm and their transfer at conception. *Sci. Rep.* **13** <https://doi.org/10.1038/s41598-023-27898-5>
35. Alshanbayeva, A., Tanwar, D. K., Roszkowski, M., Manuella, F. & Mansuy, I. M. Early life stress affects the miRNA cargo of epididymal extracellular vesicles in mouse. *Biol. Reprod.* **105**, 593–602 (2021).
36. Barrachina, F. et al. Sperm acquire epididymis-derived proteins through epididymosomes. *Hum. Reprod.* **37**, 651–668 (2022).
37. Picard, M., McEwen, B. S., Epel, E. S. & Sandi, C. An energetic view of stress: Focus on mitochondria. *Front. Neuroendocrinol.* **49**, 72–85 (2018).
38. Bobba-Alves, N., Juster, R. P. & Picard, M. The energetic cost of allostasis and allostatic load. *Psychoneuroendocrinology* **146**, 105951 (2022).
39. Picard, M. & McEwen, B. S. Psychological Stress and Mitochondria: A Conceptual Framework. *Psychosom. Med.* **80**, 126–140 (2018).
40. Picard, M., Juster, R.-P. & McEwen, B. S. Mitochondrial allostatic load puts the ‘gluc’ back in glucocorticoids. *Nature Publishing Group* <https://doi.org/10.1038/nrendo.2014.22> (2014).
41. Du, J. et al. Dynamic regulation of mitochondrial function by glucocorticoids. *Proc. Natl Acad. Sci.* **106**, 3543–3548 (2009).
42. Hunter, R. G. et al. Stress and corticosteroids regulate rat hippocampal mitochondrial DNA gene expression via the glucocorticoid receptor. *Proc. Natl Acad. Sci.* **113**, 9099–9104 (2016).
43. Lapp, H. E., Bartlett, A. A. & Hunter, R. G. Stress and glucocorticoid receptor regulation of mitochondrial gene expression. *J. Mol. Endocrinol.* **62**, R121–R128 (2019).
44. Smith, S. M. & Vale, W. W. The role of the hypothalamic-pituitary-adrenal axis in neuroendocrine responses to stress. *Dialogues Clin. Neurosci.* **8**, 383–395 (2006).
45. Spencer, R. L. & Deak, T. A users guide to HPA axis research. *Physiol. Behav.* **178**, 43–65 (2017).
46. De Kloet, E. R., Joëls, M. & Holsboer, F. Stress and the brain: from adaptation to disease. *Nat. Rev. Neurosci.* **6**, 463–475 (2005).
47. de Kloet, E. R., Karst, H. & Joels, M. Corticosteroid hormones in the central stress response: quick-and-slow. *Front Neuroendocrinol.* **29**, 268–272 (2008).
48. De Kloet, E. R., Vreugdenhil, E., Oitzl, M. S. & Joels, M. Brain Corticosteroid Receptor Balance in Health and Disease. *Endocr. Rev.* **19**, 269–301 (1998).
49. Bartlett, A. A., Lapp, H. E. & Hunter, R. G. in *Trends in Endocrinology and Metabolism* 30 807–818 (Elsevier Inc., 2019).
50. Morgan, C. P. et al. Repeated sampling facilitates within- and between-subject modeling of the human sperm transcriptome to identify dynamic and stress-responsive sncRNAs. *Sci. Rep.* **10**, 1–20 (2020).
51. Mookerjee, S. A., Gerencser, A. A., Nicholls, D. G. & Brand, M. D. Quantifying intracellular rates of glycolytic and oxidative ATP production and consumption using extracellular flux measurements. *J. Biol. Chem.* **292**, 7189–7207 (2017).
52. Hackenbrock, C. R. Ultrastructural bases for metabolically linked mechanical activity in mitochondria. *J. Cell Biol.* **30**, 269–297 (1966).
53. Mamelak, A. J. et al. Downregulation of NDUFA1 and other oxidative phosphorylation-related genes is a consistent feature of basal cell carcinoma. *Exp. Dermatol.* **14**, 336–348 (2005).
54. Au, H. C., Seo, B. B., Matsuno-Yagi, A., Yagi, T. & Scheffler, I. E. The NDUFA1 gene product (MWFE protein) is essential for activity of complex I in mammalian mitochondria. *Proc. Natl Acad. Sci.* **96**, 4354–4359 (1999).
55. Andrews, B., Carroll, J., Ding, S., Fearnley, I. M. & Walker, J. E. Assembly factors for the membrane arm of human complex I. *Proc. Natl Acad. Sci.* **110**, 18934–18939 (2013).
56. Fernandez-Moreira, D. et al. X-linked NDUFA1 gene mutations associated with mitochondrial encephalomyopathy. *Ann. Neurol.* **61**, 73–83 (2007).
57. Brand, S. R. et al. The impact of maternal childhood abuse on maternal and infant HPA axis function in the postpartum period. *Psychoneuroendocrinology* **35**, 686–693 (2010).
58. Gotlieb, N. et al. Impact of Chronic Prenatal Stress on Maternal Neuroendocrine Function and Embryo and Placenta Development During Early-to-Mid-Pregnancy in Mice. *Front Physiol.* **13**, 886298 (2022).
59. Hantsoo, L. et al. Childhood adversity impact on gut microbiota and inflammatory response to stress during pregnancy. *Brain, Behav., Immun.* **75**, 240–250 (2019).
60. Marin, M. F. et al. Chronic stress, cognitive functioning and mental health. *Neurobiol. Learn. Mem.* **96**, 583–595 (2011).
61. Miranda, J. K., de la Osa, N., Granero, R. & Ezpeleta, L. Maternal experiences of childhood abuse and intimate partner violence: Psychopathology and functional impairment in clinical children and adolescents. *Child Abus. Negl.* **35**, 700–711 (2011).
62. Morrison, K. E. et al. Pubertal adversity alters chromatin dynamics and stress circuitry in the pregnant brain. *Neuropsychopharmacology* **45**, 1263–1263 (2020).
63. Shaw, G. A. et al. Traumatic stress history interacts with sex and chronic peripheral inflammation to alter mitochondrial function of synaptosomes. *Brain Behav. Immun.* **88**, 203–219 (2020).
64. Tamashiro, K. L., Sakai, R. R., Shively, C. A., Karatsoreos, I. N. & Reagan, L. P. Chronic stress, metabolism, and metabolic syndrome. *Stress* **14**, 468–474 (2011).
65. Ziobrowski, H. N. et al. Childhood adversities and risk of post-traumatic stress disorder and major depression following a motor vehicle collision in adulthood. *Epidemiol. Psychiatr. Sci.* **32**, e1 (2023).
66. Azuma, K., Adachi, Y., Hayashi, H. & Kubo, K.-Y. Chronic Psychological Stress as a Risk Factor of Osteoporosis. *J. UOEH* **37**, 245–253 (2015).
67. De France, K., Evans, G. W., Brody, G. H. & Doan, S. N. Cost of resilience: Childhood poverty, mental health, and chronic physiological stress. *Psychoneuroendocrinology* **144**, 105872 (2022).
68. Du Preez, A. et al. Chronic stress followed by social isolation promotes depressive-like behaviour, alters microglial and astrocyte biology and reduces hippocampal neurogenesis in male mice. *Brain Behav. Immun.* **91**, 24–47 (2021).
69. Gao, X. et al. Chronic stress promotes colitis by disturbing the gut microbiota and triggering immune system response. *Proc. Natl Acad. Sci.* **115**, E2960–E2969 (2018).
70. Labanski, A., Langhorst, J., Engler, H. & Elsenbruch, S. Stress and the brain-gut axis in functional and chronic-inflammatory gastrointestinal diseases: A transdisciplinary challenge. *Psychoneuroendocrinology* **111**, 104501 (2020).

71. Le, C. P. et al. Chronic stress in mice remodels lymph vasculature to promote tumour cell dissemination. *Nat. Commun.* **7**, 10634 (2016).
72. Madhu, S. V., Siddiqui, A., Desai, N. G., Sharma, S. B. & Bansal, A. K. Chronic stress, sense of coherence and risk of type 2 diabetes mellitus. *Diabetes Metab. Syndr.* **13**, 18–23 (2019).
73. Qin, H., Lin, Z., Vásquez, E. & Xu, L. The association between chronic psychological stress and uterine fibroids risk: A meta-analysis of observational studies. *Stress Health* **35**, 585–594 (2019).
74. Scarpa, J. R. et al. Shared Transcriptional Signatures in Major Depressive Disorder and Mouse Chronic Stress Models. *Biol. Psychiatry* **88**, 159–168 (2020).
75. Steptoe, A. & Kivimäki, M. Stress and cardiovascular disease. *Nat. Rev. Cardiol.* **9**, 360–370 (2012).
76. Dearing, C., Handa, R. J. & Myers, B. Sex differences in autonomic responses to stress: implications for cardiometabolic physiology. *Am. J. Physiol. Endocrinol. Metab.* **323**, E281–E289 (2022).
77. Goldstein, J. M., Holsen, L., Handa, R. & Tobet, S. Fetal hormonal programming of sex differences in depression: linking women's mental health with sex differences in the brain across the lifespan. *Front Neurosci.* **8**, 247 (2014).
78. Kronman, H. et al. Long-term behavioral and cell-type-specific molecular effects of early life stress are mediated by H3K79me2 dynamics in medium spiny neurons. *Nat. Neurosci.* **24**, 667–676 (2021).
79. McEwen, B. S. Physiology and neurobiology of stress and adaptation: central role of the brain. *Physiol. Rev.* **87**, 873–904 (2007).
80. Cooper, T. G. et al. World Health Organization reference values for human semen characteristics. *Hum. Reprod. Update* **16**, 231–245 (2010).
81. Buck Louis, G. M. et al. Semen quality and time to pregnancy: the Longitudinal Investigation of Fertility and the Environment Study. *Fertil. Steril.* **101**, 453–462 (2014).
82. Madhusoodanan, V., Gonzalez, D. C., Jampa, A., Nassau, D. E. & Ramasamy, R. Why should we screen for male fertility? *Andrologia* **53**, <https://doi.org/10.1111/and.14218> (2021).
83. Agarwal, A., Mulgund, A., Hamada, A. & Chyatte, M. R. A unique view on male infertility around the globe. *Reproductive Biology and Endocrinology* **13**, <https://doi.org/10.1186/s12958-015-0032-1> (2015).
84. Surjit, M. et al. Widespread Negative Response Elements Mediate Direct Repression by Agonist- Liganded Glucocorticoid Receptor. *Cell* **145**, 224–241 (2011).
85. Misale, M. S., Witek Janusek, L., Tell, D. & Mathews, H. L. Chromatin organization as an indicator of glucocorticoid induced natural killer cell dysfunction. *Brain, Behav., Immun.* **67**, 279–289 (2018).
86. Krukowski, K. et al. Glucocorticoid dysregulation of natural killer cell function through epigenetic modification. *Brain, Behav., Immun.* **25**, 239–249 (2011).
87. Lempinen, J. K. & Garcia, B. A. Characterizing crosstalk in epigenetic signaling to understand disease physiology. *Biochem J.* **480**, 57–85 (2023).
88. Peng, L., Liu, X., Yang, Y., Guo, Q. & Zhong, T. Histone Deacetylase 2-Mediated Epigenetic Regulation is Involved in the Early Isoflurane Exposure-Related Increase in Susceptibility to Anxiety-Like Behaviour Evoked by Chronic Variable Stress in Mice. *Neurochem. Res.* **46**, 2333–2347 (2021).
89. Sase, A. S. et al. Sex-Specific Regulation of Fear Memory by Targeted Epigenetic Editing of Cdk5. *Biol. Psychiatry* **85**, 623–634 (2019).
90. Kobayashi, A., Azuma, K., Ikeda, K. & Inoue, S. Mechanisms Underlying the Regulation of Mitochondrial Respiratory Chain Complexes by Nuclear Steroid Receptors. *Int. J. Mol. Sci.* **21**, 6683 (2020).
91. Wiese, M. & Bannister, A. J. Two genomes, one cell: Mitochondrial-nuclear coordination via epigenetic pathways. *Mol. Metab.* **38**, 100942 (2020).
92. Mannella, C. A. The relevance of mitochondrial membrane topology to mitochondrial function. *Biochimica et Biophysica Acta - Mol. Basis Dis.* **1762**, 140–147 (2006).
93. Mannella, C. A. Structural Diversity of Mitochondria. *Ann. N. Y. Acad. Sci.* **1147**, 171–179 (2008).
94. Madrigal, J. Glutathione Depletion, Lipid Peroxidation and Mitochondrial Dysfunction Are Induced by Chronic Stress in Rat Brain. *Neuropsychopharmacology* **24**, 420–429 (2001).
95. Rezin, G. T. et al. Inhibition of mitochondrial respiratory chain in brain of rats subjected to an experimental model of depression. *Neurochem Int* **53**, 395–400 (2008).
96. Picard, M. et al. A Mitochondrial Health Index Sensitive to Mood and Caregiving Stress. *Biol. Psychiatry* **84**, 9–17 (2018).
97. Vettorazzi, S., Nalbantoglu, D., Gebhardt, J. C. M. & Tuckermann, J. A guide to changing paradigms of glucocorticoid receptor function—a model system for genome regulation and physiology. *FEBS J.* **289**, 5718–5743 (2022).
98. Cole, T. J. et al. Targeted disruption of the glucocorticoid receptor gene blocks adrenergic chromaffin cell development and severely retards lung maturation. *Genes Dev.* **9**, 1608–1621 (1995).
99. Kellendonk, C., Tronche, F., Reichardt, H. & Schutz, G. Mutagenesis of the glucocorticoid receptor in mice. *J. Steroid Biochem. Mol. Biol.* **69**, 253–259 (1999).
100. Mueller, K. M. et al. Adipocyte Glucocorticoid Receptor Deficiency Attenuates Aging- and HFD-Induced Obesity and Impairs the Feeding-Fasting Transition. *Diabetes* **66**, 272–286 (2017).
101. Whirledge, S. & DeFranco, D. B. Glucocorticoid Signaling in Health and Disease: Insights From Tissue-Specific GR Knockout Mice. *Endocrinology* **159**, 46–64 (2018).
102. Moutsatsou, P. et al. Localization of the glucocorticoid receptor in rat brain mitochondria. *Arch. Biochem Biophys.* **386**, 69–78 (2001).
103. Psarra, A. M. & Sekeris, C. E. Glucocorticoid receptors and other nuclear transcription factors in mitochondria and possible functions. *Biochim Biophys. Acta* **1787**, 431–436 (2009).
104. Psarra, A. M. & Sekeris, C. E. Glucocorticoids induce mitochondrial gene transcription in HepG2 cells: role of the mitochondrial glucocorticoid receptor. *Biochim Biophys. Acta* **1813**, 1814–1821 (2011).
105. Bestwick, M. L. & Shadel, G. S. Accessorizing the human mitochondrial transcription machinery. *Trends Biochemical Sci.* **38**, 283–291 (2013).
106. Basarrate, S. et al. Glucocorticoid and Adrenergic Receptor Distribution Across Human Organs and Tissues: A Map for Stress Transduction. *Psychosom. Med* **86**, 89–98 (2024).
107. Zhao, R. Z., Jiang, S., Zhang, L. & Yu, Z. B. Mitochondrial electron transport chain, ROS generation and uncoupling (Review). *Int. J. Mol. Med.* **44**, 3–15 (2019).
108. Mathieu, M., Martin-Jaular, L., Lavieu, G. & Théry, C. Specificities of secretion and uptake of exosomes and other extracellular vesicles for cell-to-cell communication. *Nat. Cell Biol.* **21**, 9–17 (2019).
109. Morrison, K. E. et al. Developmental Timing of Trauma in Women Predicts Unique Extracellular Vesicle Proteome Signatures. *Biol. Psychiatry* **91**, 273–282 (2022).
110. Van Niel, G., D'Angelo, G. & Raposo, G. Shedding light on the cell biology of extracellular vesicles. *Nat. Rev. Mol. Cell Biol.* **19**, 213–228 (2018).
111. Rowlison, T., Cleland, T. P., Ottinger, M. A. & Comizzoli, P. Novel Proteomic Profiling of Epididymal Extracellular Vesicles in the Domestic Cat Reveals Proteins Related to Sequential Sperm Maturation with Differences Observed between Normospermic and Teratospermic Individuals. *Mol. Cell. Proteom.: MCP* **19**, 2090–2103 (2020).

112. Chen, F. et al. Extracellular vesicle-packaged HIF-1 $\alpha$ -stabilizing lncRNA from tumour-associated macrophages regulates aerobic glycolysis of breast cancer cells. *Nat. Cell Biol.* **21**, 498–510 (2019).
113. Durairajanayagam, D., Singh, D., Agarwal, A. & Henkel, R. Causes and consequences of sperm mitochondrial dysfunction. *Andrologia* **53**, <https://doi.org/10.1111/and.13666> (2021).
114. Irigoyen, P. et al. Mitochondrial metabolism determines the functional status of human sperm and correlates with semen parameters. *Front Cell Dev. Biol.* **10**, 926684 (2022).
115. Moscatelli, N. et al. Single-cell-based evaluation of sperm progressive motility via fluorescent assessment of mitochondria membrane potential. *Sci. Rep.* **7**, <https://doi.org/10.1038/s41598-017-18123-1> (2017).
116. Wang, J.-J. et al. Age-Related Decline of Male Fertility: Mitochondrial Dysfunction and the Antioxidant Interventions. *Pharmaceuticals* **15**, 519 (2022).
117. Amaral, A., Lourenço, B., Marques, M. & Ramalho-Santos, J. Mitochondria functionality and sperm quality. *REPRODUCTION* **146**, R163–R174 (2013).
118. Kasai, T. et al. Relationship between sperm mitochondrial membrane potential, sperm motility, and fertility potential. *Asian J. Androl.* **4**, 97–103 (2002).
119. Danshina, P. V. et al. Phosphoglycerate Kinase 2 (PGK2) Is Essential for Sperm Function and Male Fertility in Mice. *Biol. Reprod.* **82**, 136–145 (2010).
120. Practice Committees of the American Society for Reproductive Medicine & the Society for Reproductive Biologists and Technologists. Comprehensive guidance for human embryology, andrology, and endocrinology laboratories: management and operations: a committee opinion. *Fertil Steril.* **117**, 1183–1202 (2022).
121. Felitti, V. J. et al. Relationship of Childhood Abuse and Household Dysfunction to Many of the Leading Causes of Death in Adults. *Am. J. Preventive Med.* **14**, 245–258 (1998).
122. Sheehan, D. V. et al. The Mini-International Neuropsychiatric Interview (M.I.N.I.): The Development and Validation of a Structured Diagnostic Psychiatric Interview for DSM-IV and ICD-10. *J. Clin. Psychiatry* **59**, quiz 34–57 (1998).
123. Cohen, S., Kamarck, T. & Mermelstein, R. A Global Measure of Perceived Stress. *J. Health Soc. Behav.* **24**, 385–396 (1983).
124. WHO. WHO laboratory manual for the examination and processing of human semen, sixth edition. (2021).
125. Pinheiro, J. & Bates, D. *Mixed-Effects Models in S and S-PLUS*. (Springer, 2000).
126. nlme: Linear and Nonlinear Mixed Effects Models v. R package version 3.1–163 (2023).
127. Fox, J. Effect Displays in R for Generalized Linear Models. *J. Stat. Softw.* **8**, 1–27 (2003).
128. Fox, J. & Weisberg, S. *An R Companion to Applied Regression, 3rd edition*. (Sage, 2019).
129. Araki, Y., Suzuki, K., Matusik, R. J., Obinata, M. & Orgebin-Crist, M. C. Immortalized Epididymal Cell Lines From Transgenic Mice Overexpressing Temperature-Sensitive Simian Virus 40 Large T-Antigen Gene. *J. Androl.* **23**, 854–869 (2002).
130. Skene, P. J., Henikoff, J. G. & Henikoff, S. Targeted in situ genome-wide profiling with high efficiency for low cell numbers. *Nat. Protoc.* **13**, 1006–1019 (2018).
131. Skene, P. J. & Henikoff, S. An efficient targeted nuclease strategy for high-resolution mapping of DNA binding sites. *eLife* **6**, <https://doi.org/10.7554/eLife.21856> (2017).
132. Bray, N. L., Pimentel, H., Melsted, P. & Pachter, L. Near-optimal probabilistic RNA-seq quantification. *Nat. Biotechnol.* **34**, 525–527 (2016).
133. Church, D. M. et al. Modernizing Reference Genome Assemblies. *PLoS Biol.* **9**, e1001091 (2011).
134. Divakaruni, A. S. et al. Thiazolidinediones are acute, specific inhibitors of the mitochondrial pyruvate carrier. *Proc. Natl Acad. Sci.* **110**, 5422–5427 (2013).
135. Taniguchi, H. et al. Establishment of a novel assessment of the quality of human spermatozoa measuring mitochondrial oxygen metabolism. *BMC Research Notes* **15**, <https://doi.org/10.1186/s13104-022-06012-4> (2022).
136. Kim, C. et al. Comparative Analysis of the Mitochondrial Physiology of Pancreatic  $\beta$  Cells. *Bioenergetics: Open Access* **03**, <https://doi.org/10.4172/2167-7662.1000110> (2014).
137. Schneider, S. S. et al. Individual-specific variation in the respiratory activities of HMECs and their bioenergetic response to IGF1 and TNF $\alpha$ . *J. Cell. Physiol.* **232**, 2750–2765 (2017).
138. Clayton, D. A. & Shadel, G. S. Isolation of Mitochondria from Tissue Culture Cells. *Cold Spring Harb. Protoc.* **2014**, pdb.prot080002 (2014).
139. Compton, S. et al. Mitochondrial dysfunction impairs tumor suppressor p53 expression/function. *J. Biol. Chem.* **286**, 20297–20312 (2011).
140. Yadava, N., Houchens, T., Potluri, P. & Scheffler, I. E. Development and characterization of a conditional mitochondrial complex I assembly system. *J. Biol. Chem.* **279**, 12406–12413 (2004).
141. Yadava, N., Potluri, P., Smith, E. N., Bisevac, A. & Scheffler, I. E. Species-specific and mutant MWFE proteins. Their effect on the assembly of a functional mammalian mitochondrial complex I. *J. Biol. Chem.* **277**, 21221–21230 (2002).
142. Picard, M., White, K. & Turnbull, D. M. Mitochondrial morphology, topology, and membrane interactions in skeletal muscle: A quantitative three-dimensional electron microscopy study. *J. Appl. Physiol.* **114**, 161–171 (2013).
143. Ramirez, M. I. et al. Technical challenges of working with extracellular vesicles. *Nanoscale* **10**, 881–906 (2018).
144. Théry, C. et al. Minimal information for studies of extracellular vesicles 2018 (MISEV2018): a position statement of the International Society for Extracellular Vesicles and update of the MISEV2014 guidelines. *J. Extracell. Vesicles* **7**, 1535750 (2018).
145. Hoyt, J. M. et al. The SEK-1 p38 MAP Kinase Pathway Modulates Gq Signaling in *Caenorhabditis elegans*. *G3 Genes|Genomes|Genet.* **7**, 2979–2989 (2017).
146. Langmead, B. & Salzberg, S. L. Fast gapped-read alignment with Bowtie 2. *Nat. Methods* **9**, 357–359 (2012).
147. Meers, M. P., Bryson, T. D., Henikoff, J. G. & Henikoff, S. Improved CUT&RUN chromatin profiling tools. *eLife* **8**, <https://doi.org/10.7554/eLife.46314> (2019).
148. Ross-Innes, C. S. et al. Differential oestrogen receptor binding is associated with clinical outcome in breast cancer. *Nature* **481**, 389–393 (2012).
149. Wang, Q. et al. Exploring Epigenomic Datasets by ChIPseeker. *Curr. Protoc.* **2**, e585 (2022).
150. Yu, G., Wang, L.-G. & He, Q.-Y. ChIPseeker: an R/Bioconductor package for ChIP peak annotation, comparison and visualization. *Bioinformatics* **31**, 2382–2383 (2015).
151. Afgan, E. et al. The Galaxy platform for accessible, reproducible and collaborative biomedical analyses: 2016 update. *Nucleic Acids Res* **44**, W3–w10 (2016).
152. Ramírez, F., Dündar, F., Diehl, S., Grüning, B. A. & Manke, T. deepTools: a flexible platform for exploring deep-sequencing data. *Nucleic Acids Res* **42**, W187–191 (2014).
153. Kent, W. J. et al. The Human Genome Browser at UCSC. *Genome Res.* **12**, 996–1006 (2002).
154. Nassar, L. R. et al. The UCSC Genome Browser database: 2023 update. *Nucleic Acids Res.* **51**, D1188–D1195 (2022).

155. Berry, A. S. F. et al. An Open-Source Toolkit To Expand Bioinformatics Training in Infectious Diseases. *mBio* **12**, e0121421 (2021).
156. Sonesson, C., Love, M. I. & Robinson, M. D. Differential analyses for RNA-seq: transcript-level estimates improve gene-level inferences. *F1000Research* **4**, 1521 (2015).
157. Robinson, M. D., McCarthy, D. J. & Smyth, G. K. edgeR: a Bioconductor package for differential expression analysis of digital gene expression data. *Bioinformatics* **26**, 139–140 (2010).
158. Ritchie, M. E. et al. limma powers differential expression analyses for RNA-sequencing and microarray studies. *Nucleic Acids Res.* **43**, e47–e47 (2015).
159. Langfelder, P. & Horvath, S. WGCNA: an R package for weighted correlation network analysis. *BMC Bioinforma.* **9**, 559 (2008).
160. Storey, J. D. A direct approach to false discovery rates. *J. R. Stat. Soc. Ser. B: Stat. Methodol.* **64**, 479–498 (2002).
161. Zhang, B. & Horvath, S. A General Framework for Weighted Gene Co-Expression Network Analysis. *Statistical Applications in Genetics and Molecular Biology* **4**, <https://doi.org/10.2202/1544-6115.1128> (2005).
162. Huang da, W., Sherman, B. T. & Lempicki, R. A. Bioinformatics enrichment tools: paths toward the comprehensive functional analysis of large gene lists. *Nucleic Acids Res* **37**, 1–13 (2009).
163. Huang, D. W., Sherman, B. T. & Lempicki, R. A. Systematic and integrative analysis of large gene lists using DAVID bioinformatics resources. *Nat. Protoc.* **4**, 44–57 (2009).

## Acknowledgements

We thank the University of Maryland Electron Microscopy Core Imaging Facility for transmission electron microscopy consultation and training, Nagendra Yadava and Brandon Carter-Cooper at the University of Maryland Translational Laboratory Shared Service for respirometry consultation, the Ndufa1 antibody, and recombinant perfringolysin O, Amanda Law for shared equipment, Victoria Meadows, Jessica Fluharty, Henry Haller, Erin Weinhold, and Peter Moon for technical assistance, and Scott Thompson for editorial feedback. We thank the University of Colorado Neuroscience Program and University of Colorado and University of Maryland Medical Scientist Training Programs for their support. This work was supported by the National Institutes of Health grant MH129495 (T.L.B.), National Institutes of Health grant HD097093 (T.L.B.), National Institutes of Health grant MH108286 (T.L.B.), National Institutes of Health grant HD105771 (T.L.B and N.E.).

## Author contributions

Conceptualization: N.M., C.P.M, and T.L.B.; methodology: N.M., C.P.M. C.M., M.S., N.E., and T.L.B.; software: N.M., C.P.M., and R.J.; formal

analysis: N.M., and R.J.; investigation: N.M., C.P.M, R.M.R., A.J. and I.C.; writing—original draft: N.M. and T.L.B.; writing—review and editing: N.M., C.M., A.J., and T.L.B.; funding acquisition, T.L.B. and N.E.

## Competing interests

The authors declare no competing interests.

## Additional information

**Supplementary information** The online version contains supplementary material available at <https://doi.org/10.1038/s41467-024-52319-0>.

**Correspondence** and requests for materials should be addressed to Tracy L. Bale.

**Peer review information** *Nature Communications* thanks Anthony Hannan, and the other, anonymous, reviewers for their contribution to the peer review of this work. A peer review file is available.

**Reprints and permissions information** is available at <http://www.nature.com/reprints>

**Publisher's note** Springer Nature remains neutral with regard to jurisdictional claims in published maps and institutional affiliations.

**Open Access** This article is licensed under a Creative Commons Attribution-NonCommercial-NoDerivatives 4.0 International License, which permits any non-commercial use, sharing, distribution and reproduction in any medium or format, as long as you give appropriate credit to the original author(s) and the source, provide a link to the Creative Commons licence, and indicate if you modified the licensed material. You do not have permission under this licence to share adapted material derived from this article or parts of it. The images or other third party material in this article are included in the article's Creative Commons licence, unless indicated otherwise in a credit line to the material. If material is not included in the article's Creative Commons licence and your intended use is not permitted by statutory regulation or exceeds the permitted use, you will need to obtain permission directly from the copyright holder. To view a copy of this licence, visit <http://creativecommons.org/licenses/by-nc-nd/4.0/>.

© The Author(s) 2024